The Aeronautical Journal (2024), **128**, pp. 441–468
doi:10.1017/aer.2023.62

ROYAL AERONAUTICAL SOCIETY

REGULAR PAPER

Numerical investigation of the dynamic stall reduction on the UAS-S45 aerofoil using the optimised aerofoil method

M. Bashir[1], N. Zonzini[2], S. Longtin Martel[1], R.M. Botez[1], A. Ceruti[2] and T. Wong[1]

[1]École de Technolgie Supérieure, Department of Systems Engineering, Research Laboratory in Active Controls, Avionics and Aeroservoelasticity (LARCASE), 1100 Notre-Dame West, Montreal, QC, Canada, H3C1K3 and [2]Department of Industrial Engineering, University of Bologna, Italy
Corresponding author: R. Mihaela Botez; Email: ruxandra.botez@etsmtl.ca

Received: 19 October 2022; **Revised:** 22 June 2023; **Accepted:** 30 June 2023

Keywords: optimization; morphing leading edge; morphing trailing edge; dynamic stall; reduced frequency; laminar separation bubble

Abstract

This paper investigates the effect of the optimised morphing leading edge (MLE) and the morphing trailing edge (MTE) on dynamic stall vortices (DSV) for a pitching aerofoil through numerical simulations. In the first stage of the methodology, the optimisation of the UAS-S45 aerofoil was performed using a morphing optimisation framework. The mathematical model used Bezier-Parsec parametrisation, and the particle swarm optimisation algorithm was coupled with a pattern search with the aim of designing an aerodynamically efficient UAS-45 aerofoil. The $\gamma - Re_{\theta}$ transition turbulence model was firstly applied to predict the laminar to turbulent flow transition. The morphing aerofoil increased the overall aerodynamic performances while delaying boundary layer separation. Secondly, the unsteady analysis of the UAS-S45 aerofoil and its morphing configurations was carried out and the unsteady flow field and aerodynamic forces were analysed at the Reynolds number of 2.4×10^6 and five different reduced frequencies of $k = 0.05$, 0.08, 1.2, 1.6 and 2.0. The lift (C_L), drag (C_D) and moment (C_M) coefficients variations with the angle-of-attack of the reference and morphing aerofoils were compared. It was found that a higher reduced frequencies of 1.2 to 2 stabilised the leading-edge vortex that provided its lift variation in the dynamic stall phase. The maximum lift $\left(C_{L,max}\right)$ and drag $\left(C_{D,max}\right)$ coefficients and the stall angles of attack are evaluated for all studied reduced frequencies. The numerical results have shown that the new radius of curvature of the MLE aerofoil can minimise the streamwise adverse pressure gradient and prevent significant flow separation and suppress the formation of the DSV. Furthermore, it was shown that the morphing aerofoil delayed the stall angle-of-attack by 14.26% with respect to the reference aerofoil, and that the $C_{L,max}$ of the aerofoil increased from 2.49 to 3.04. However, while the MTE aerofoil was found to increase the overall lift coefficient and the $C_{L,max}$, it did not control the dynamic stall. Vorticity behaviour during DSV generation and detachment has shown that the MTE can change the vortices' evolution and increase vorticity flux from the leading-edge shear layer, thus increasing DSV circulation. The conclusion that can be drawn from this study is that the fixed drooped morphing leading edge aerofoils have the potential to control the dynamic stall. These findings contribute to a better understanding of the flow analysis of morphing aerofoils in an unsteady flow.

Nomenclature

α	angle-of-attack
α_m	mean incidence angle
α_a	amplitude incidence angle
C_L	lift coefficient
$C_{L,max}$	maximum lift coefficient
C_D	drag coefficient
$C_{D,max}$	maximum drag coefficient

c	chord
C_P	pressure coefficient
k	reduced frequency
t	time
U_∞	freestream velocity
LEV	leading edge vortex
TEV	trailing edge vortex
DSV	dynamic stall vortex
MLE	morphing leading edge
MTE	morphing trailing edge

1.0 Introduction

The increasing demand for air transportation has heightened environmental concerns and put a strain on the aircraft sector. Due to the unpredictability of fuel costs and growing environmental concerns, fuel efficiency has become a critical element in aircraft design. In 2020, the global aviation industry was predicted to surpass 40.3 million commercial flights, a 50% increase over the previous decade. The aviation industry's main objectives are to improve the quality and affordability of air transportation, to mitigate its environmental impact by reducing CO_2, NO_X, fossil fuels consumption and noise emissions, and to address safety problems [1]. These goals have resulted in an increasing demand for novel research ideas aimed at developing more efficient and environmentally friendly aircraft. Moreover, all the new studies dealing with the use of batteries for electric flight, new biofuels and hydrogen suggest the need for the increase of the aerodynamic efficiency in terms of energy to weight ratio. Aircraft configurations with higher efficiency could anticipate the batteries development level required for effective operations. Several significant collaborations have been established between industry, academia and research institutions to design, manufacture and test innovative morphing technologies with the aim of reducing emissions [2–4]. Numerous investigations at the Research Laboratory in Active Controls, Avionics, and AeroServoElasticity (LARCASE) have explored potential ways for reducing aircraft fuel consumption and increasing the aerodynamic efficiency, including experimental investigations of morphing wing models [5–11]. Figure 1 shows the Price-Païdoussis subsonic blow down wind tunnel used to carry out the LARCASE experimental studies. Different metaheuristic optimisation algorithms to improve the flight phase cost in terms of fuel burn have been studied for commercial aircraft models [12, 13]. Some of the algorithms implemented for different optimisation strategies are genetic algorithms, the artificial bee colony and the ant colony algorithm.

Morphing can increase an aircraft's performance in terms of lift, drag and noise by removing wing surface discontinuities and gaps [14–19], thus obtaining a smooth surface. Nowadays aircraft are designed to produce maximum aerodynamic performance (highest lift-to-drag ratio) within a flight envelope. Moreover, the maximum efficiency is not typically reached during the cruise because it requires a speed which is often too reduced, so that a trade-off between performances and operational needs must be defined. However, mission criteria vary continuously during flight phases, and an aircraft frequently flies in suboptimal conditions. Although typical aircraft are equipped with hinged lifting mechanisms and trailing edge surfaces to manage airflow, these aircraft may generate surface discontinuities and increase drag [3, 20]. These hinged surfaces have drawbacks in both their deployed and retracted states [21]. If the high lifting surface is not aligned properly, it can induce noise, turbulence and a turbulent boundary layer, thus increasing the drag. Moreover, also from a structural point of view, moving surfaces require complex mechanisms and in the case of the flaps usually only few deflection positions can be set by pilots in commercial aircraft. Many experts claim that laminarisation technology can reduce drag and prevent flow separation [22–24]. The morphing leading edge device is a gapless flexible droop nose that undergoes a substantial shape and camber alteration. The actuation system can lie within the aerofoil, thus avoiding the need for external mechanisms and fairings. Various advanced device concepts

https://doi.org/10.1017/aer.2023.62 Published online by Cambridge University Press

Figure 1. *LARCASE Price-Païdoussis subsonic blow down wind tunnel.*

have been studied in detail considering both aerodynamic performance assessment and aeroelastic wing deflection effects [25–27].

Unsteady aerodynamic analysis plays an important role in the process of conceptual morphing designs. Morphing optimisation has revealed that optimised lift and drag coefficients can be obtained at different flight conditions. The use of morphing wing technology as a flow control technique has resulted in efficient aerodynamic designs [15, 28–30]. Dynamic stall control is especially significant because it occurs in all aerospace applications, such as on UAVs [31, 32], helicopter rotors [33, 34], wind turbines [35, 36] and military aircraft [37, 38]. The effects of unsteady parameters, such as the oscillation amplitude, reduced frequency, Reynolds number and aerofoil kinematics (deformation, variable thickness etc.) have been investigated by different researchers from the perspective of aerodynamic coefficients [39–42]. Numerical studies were used to investigate morphing wing aerodynamic stall and to explore adaptive morphing trailing-edge wings, 1% drag reduction on-design and 5% off-design were obtained [43]. A hybrid RANS-LES technique was used to investigate the aerodynamic performance of an aerofoil with a downward, statically morphing trailing-edge flap (TEF). Morphing enhanced lift-to-drag by 6% [44, 45]. Similar results were reported for the aerodynamic and aeroacoustics responses of an aerofoil fitted with a harmonically morphing trailing edge flap [46]. It is worth noting that a slight increase in efficiency impacts with a magnification factor the maximum take off (MTO) mass of an aircraft by reducing in a significant way the fuel consumption. Moreover, RANS numerical simulations of a NACA0012 aerofoil with a flexible trailing-edge showed that the morphing surface can delay the beginning of flow separation with the aim to achieve optimal aerodynamic performance [47, 48].

The dynamic stall is an aerodynamic phenomenon that occurs when the flow over the wings and aerodynamic bodies separates rapidly due to changes in relative freestream conditions. Dynamic stall is marked by increased flow-field unsteadiness, resulting in increased airframe vibration and reduced aerodynamic performance [49, 50]. A thin reversed flow region forms at the trailing edge before dynamic stall. A reverse pressure gradient moves the reversed flow area to the leading edge, while the flow remains attached. The leading edge of the vortex produces a powerful suction. A leading-edge vortex (LEV) progressively splits from the aerofoil surface to generate a dynamic stall vortex (DSV). The DSV develops near the trailing edge as the angle-of-attack increases, resulting in aerodynamic moment variations. For a higher angle-of-attack, the DSV separates from the trailing edge of the aerofoil.

Both dynamic and static stall produces significant losses in lift and large increases in drag. The dynamic stall has the added feature of generating significant negative pitching moments. These large pitching moments and the associated negative damping of the cycle cause high torsional stresses in a helicopter rotor blade, which can lead to its destruction. The dynamic stall phenomenon, which is the

https://doi.org/10.1017/aer.2023.62 Published online by Cambridge University Press

process of delayed flow separation brought on by a quick change in the angle-of-attack of rotating blades, significantly impacts the performance parameters of vertical axis wind turbines. Low tip speed ratios, where unstable flow separation and dynamic stall dominate the blade aerodynamics, cause the wind turbines to perform poorly in terms of power output.

Numerous flow control devices have been developed to avoid flow separation and to mitigate dynamic stall effects. They can be classified as active, or passive based on their operational properties. Vortex generators, micro-tabs, and serrated trailing edges are all examples of passive control devices. Active control mechanisms include trailing-edge flaps and synthetic jets of fluids. The use of leading-edge slats [51, 52], trailing-edge flaps [53, 54], synthetic jet/periodic excitation strategies [55–57], plasma actuators [58], vortex generators [59], and dynamically morphing leading-edge [60] has been studied. In a wind tunnel, a morphing wing was optimised in real time to delay the flow transition to the trailing edge [61]. The upper surface of the morphing rectangular finite aspect ratio wing was designed using a flexible composite material, and it was further equipped with pressure sensors and two smart memory alloy actuators. The morphing wing was obtained using several optimiaed aerofoils by controlling the two actuators' strokes automatically. It was demonstrated in this study that the optimisation mechanism in the control software code allowed the morphing wing to optimise its shape for various flight cases.

Studies for dynamic stall reduction using flow control have been done in the literature. These studies included the use of aerofoil leading or trailing edge flaps [53, 62], vortex generators [63], zero mass jets [64], flow blowing and sucking devices [65] etc. The high-frequency control techniques for dynamic stall control gave the benefits of instabilities associated with the laminar separation bubble (LSB) to delay the occurrence of a dynamic stall vortex (DSV) [66, 67]. The authors mentioned that the substantial negative pitching moment and its associated aerodynamic damping properties were obtained because of the trailing edge vortex. The TE flaps dynamics was investigated using the dynamic loads generated through oscillating aerofoils [67].

The use of a leading-edge slat device for dynamic stall control was investigated numerically using a two-dimensional Navier–Stokes solver for multi-element aerofoils [68]. Another option is to use suction/blowing. Blowing slots were set at 10% and 70% of the chord to conduct a dynamic-stall control test. Sun and Sheikh numerically simulated dynamic-stall control with near-leading-edge tangential blowing [69].

A deployable leading edge vortex generator was used in an active dynamic stall control approach [70]. Wind tunnel studies have shown that the device delayed the static stall and reduced dynamic stall penalties. Three degrees were added to the static stall angle. The dynamic stall reduced the negative pitching moment peak by 60% [46]. Numerical studies evaluated the impact of the synthetic jet control on the unstable dynamic stall over a rotor aerofoil [71]. It was shown that the jets were most efficient when the stall was located at the flow separation point. Adjusting jet angle and momentum coefficients had similar impacts on dynamic stall characteristics. When situated near the flow separation point, a modest jet angle offered the optimum control effects on aerofoil aerodynamic forces. In the separated flow region, a medium-angle synthetic jet is more effective. Experimental investigations using plasma-based devices or other high-frequency actuation were carried out using employing high-fidelity wall-resolved large-eddy simulations [66, 72].

The effects of the trailing edge flap (TEF) flow control on helicopter rotor blade dynamic stall were explored in Ref. (73). The authors found that the substantial negative pitching moments and their related negative aerodynamic damping were caused by the trailing edge vortex: and its only upward flap deflections reduced aerodynamic damping. Another study examined the outcome of the TEF and LEF on the dynamic loads generated by an oscillating aerofoil [74, 75].

The study indicated that the downward LEF motion suppressed leading edge separation and eliminated the occurrence of the DSV, leading to a minor reduction in $C_{L,max}$ but a considerably improved post stall lift condition, compared with the baseline aerofoil. The joint upward LEF and downward TEF control produced the largest $C_{L,max}$. Another investigation was carried out to study the effect of a TEF on dynamic stall of wind turbine blades [76]. The TEF reduced lift and root bending moment by 26% and 24%, respectively. These results show how TEF reduced wind turbine blade loads changes. Another

https://doi.org/10.1017/aer.2023.62 Published online by Cambridge University Press

study analysed the flow field around a helicopter blade in forward flight [77]. The two-dimensional model incorporated forward flight speed, resulting in a time-variable aerofoil flow speed. Therefore, phenomena such as shock wave near the leading-edge of aerofoil, which is critical to dynamic stall formation, were modeled using more realistic flow conditions. This study examined aerofoil nose drooping and showed that it reduces and alleviates dynamic stall. An aerofoil can be drooped to eliminate shock wave from its leading edge, and therefore no dynamic stall will occur.

Therefore, the literature mentioned above has proven mainly those different methods can be implemented to control the dynamic stall of the pitching aerofoil. In this paper, the attention is focused on the morphing aerofoil deformations, which are done in the frame of one of the most promising methods available to control the dynamic stall. However, dynamic aerofoil morphing phenomena imposes a significant amount of complexity in the structure and control systems of a morphing wing. Therefore, the first objective of this study is to obtain optimised aerofoils for the (MLE and the MTE to enhance the overall aerodynamic performance. The obtained optimised aerofoils are then evaluated to investigate the dynamic stall. To our knowledge, only a few numerical studies have used optimised aerofoils to model the dynamic stall phenomenon at a moderate Reynolds number turbulent flow regime. Transition SST model's ability to predict laminar, transitional and fully turbulent flow regimes will contribute to a better understanding of the flow physics of dynamic stall and its delay. The paper is structured as follows Section 2 describes the methodology developed to optimise the aerofoil, Section 3 includes a discussion of the results obtained in Section 2. Finally, Section 4 describes the outcome of this study and future work that could be carried out to investigate the dynamic stall.

2.0 Methodolgy

2.1 Optimisation problem definition

The MLE and MTE aerofoils derived from the UAS-S45 aerodynamic shape have been obtained through an optimisation by using an intelligent and iterative approach based on user-defined aerodynamics and constraints. In the aerodynamic technique used here, an objective function formulation was coupled with a geometrical shape parameterisation model, an aerodynamic flow solver and an optimisation algorithm. All these mathematical tools have been combined together in order to find a solution. Different morphing aerofoil shapes were obtained for improving the UAV's aerodynamic performance.

An optimisation framework was developed for this study to allow the integration of aerofoil generation via the direct manipulation of the aerofoil shape variables while respecting to geometrical limitations. Figure 2 depicts the optimisation approach structure, which includes a geometrical modelling block based on the Bezier-PARSEC (BP) parameterisation technique and an aerodynamic solver, namely the panel solver XFOIL. The Transition SST model's results are validated using a high-fidelity solver in Ansys Fluent, based on Reynolds-Averaged Navier–Stokes (RANS) equations. A hybrid optimiser is also utilised, which combines the particle swarm optimization (PSO) method with the pattern search (PS) technique. The optimisation procedure is presented in more details [7].

The ability to search and obtain the best solution is demonstrated by designing an optimised aerofoil derived from the UAS-S45 aerofoil, with the goal of maximiaing lift-to-drag ratio at cruise speed. For this design challenge, the following optimiaation function was constructed as shown in Equation (1):

$$maximize\, f(x) = \frac{C_L}{C_D}(X);\ X \in (air\ foil\ set) \tag{1}$$

such that:

$$C_{Lmax} \geqslant C_{Lmax(baseline\ airfoil)}$$

$$X \in (airfoil\ set)\ \text{ such that } \mathrm{LB} \leq \mathrm{X} \leq \mathrm{UB}$$

where N is the number of flight conditions for which the objective function is maximised, LB is the lower bound and UB is the upper bound.

https://doi.org/10.1017/aer.2023.62 Published online by Cambridge University Press

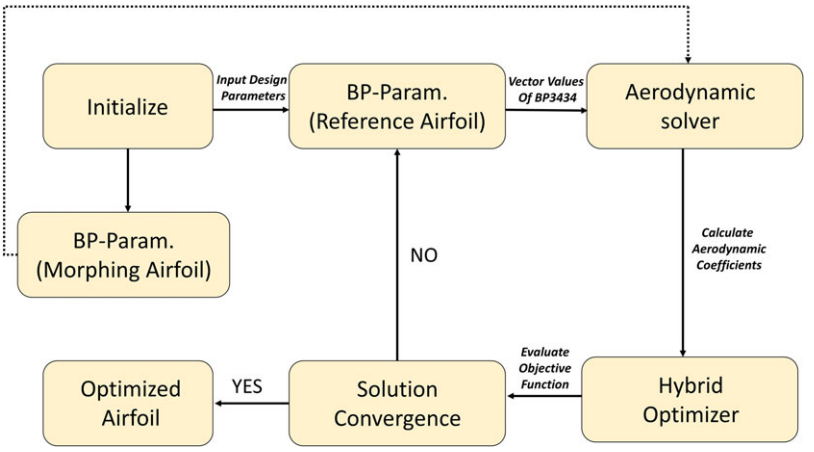

Figure 2. *Schematics of the optimisation procedure [7].*

The geometrical parameterisation is one of the most important aspects of the aerofoil shape optimisation and design. By optimising both the geometric and aerodynamic properties, the parameterised aerofoil should have a small number of design variables. The number of design variables can be increased, which will take a long time and require high computing resources [78]. There are numerous methods available for the shape parameterisation of aerofoils geometries. Some of the well-known methods are discrete points, Bezier or B-Spline, free-form representation and cubic spline control point representation [78, 79]. These methods have the disadvantages such as the method does not use aerofoil parameters as design variables, requiring a large number of design variables than those of the aerofoil parameters, and they frequently produce erroneous shapes for aerofoil's leading and trailing edges. The main problem needed to solve is to find a mathematical description of the aerofoil based on the positions of a limited set of points, whose positions are changed by the optimisation algorithm.

The BP parameterisation was developed by Derksen and Rogalsky, and describes Bezier curves using PARSEC parameterizations [80]. It is classified into BP3333 and BP3434. The BP3333 uses third-order Bezier curves for the aerofoil camber and thickness, and its key advantages are of close relevance to aerofoil aerodynamic parameters, fast optimisation, continuity features low number of design variation and avoidance of abrupt leading edges. Reduced degree of freedom prevents the parameterisation of camber trailing edge aerofoils. In the BP3434, third-order Bezier curves define the camber and thickness of the aerofoil's leading edge, whereas fourth-order Bezier curves define the trailing edge, as shown in Fig. 3. When an aerofoil's camber is negative along its chord, the BP3434 is more efficient than BP3333, and therefore the BP3434 type is implemented in this study.

It is worth noting that Bezier curves are not defined by a set of interpolating points from which the curve passes through, but by a control polygon; the shape of the curve is managed by changing the positions of the points of the control polygon. However, the BP method's inverse design problem does not have enough potential for accelerated convergence when parameterisation is considered while determining algorithm robustness and convergence rate. In addition, higher-order Bezier curves are required for better solutions, such as BP 3434, which is more robust than BP 3333, and some of these curves will contribute in a non-linear way to the objective function.

For the UAS-S45 aerofoil optimisation, a hybrid optimiser based on the (PSO method combined with the PS algorithm was employed to improve the solution convergence and refinement. The PSO technique is based on the imitation of flock of birds or school of fish while searching for food, with solutions represented by particles that heuristically search a design space.

The hybrid optimisation approach initially uses the PSO to optimise all variables. A second optimiser is then applied to the PSO's output due to small particles motion and their positions near optimised values or patterns. PSO is followed by PS optimisation. The PS can identify a local optimum in a confined

https://doi.org/10.1017/aer.2023.62 Published online by Cambridge University Press

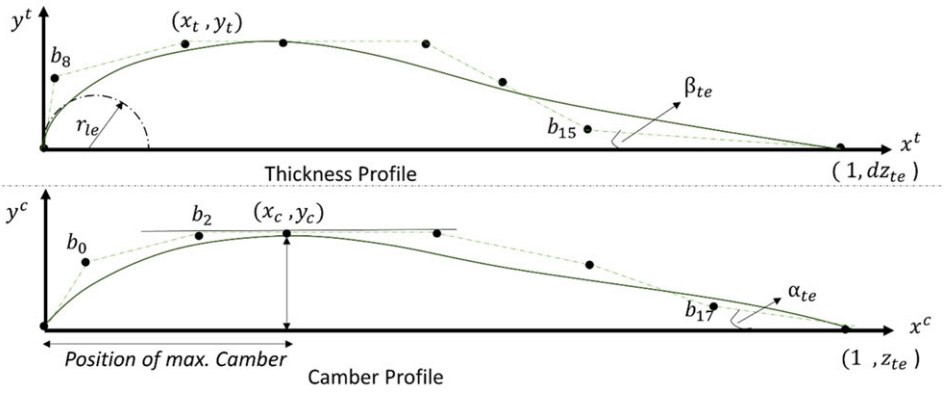

Figure 3. *BP3434 parameterisation scheme defining the Bezier aerofoil curves.*

search region; the coupled use of PSO-PS provides better results than a single optimiser. One of the problems of heuristic optimisation is the local minimum solution: such an algorithm can find a sub-optimal solution and not find the zones of the design space where the best solution lies. The optimisation procedure generates a cost for every tested configuration by use of an objective function and a penalty function with the aim to remove non-realistic or non-feasible solutions from possible optimisation results. Upper and lower bounds control the number of input variables. These bounds ensure that the search space for both the PSO and the PS remain within them. During the PSO execution, if a particle is outside the search space constraints, its value is replaced by that of the within bound.

2.2 Unsteady analysis using Computational Fluid Dynamics (CFD) solver

For the pitching aerofoil dynamiccases, the Reynolds number based on the aerofoil chord length is $\mathrm{Re} = 2.4 \times 10^6$. During dynamic simulations, the aerofoil undergoes a sinusoidal pitching motion, as shown in Equation (2):

$$\alpha\,(t) = \alpha_m + \alpha_a \sin\,(\omega t) \tag{2}$$

where $\alpha_m = 11^\circ$ is the mean incidence angle, $\alpha_a = 20^\circ$ is the amplitude, f is the aerofoil oscillation frequency and t is the time.

The reduced frequency k is defined in Equation (3):

$$k = \frac{\omega c}{2U_\infty} \tag{3}$$

where U_∞ is the freestream velocity, and c is the aerofoil chord length. Various reduced frequencies k were chosen for the aerofoil and the Reynolds number based on the unit chord length and free-stream velocity of 35.5 m/s was set to 2.4×10^6.

2.2.1 Computational domain and grid

The computational domain is 20c (20 times the length of the aerofoil chord) upstream and 30c downstream of the aerofoil pitch axis, while the inner circular region is 5c in diameter and centered at 0.25c aft of the leading edge. The mesh employs sliding mesh to obtain the aerofoil pitching motion to avoid re-meshing, and to maintain cells quality. This work focusses on the pitching mode denoted by $\alpha\,() = 11 + 15\sin\,(\omega t)$ in which the aerofoil enters a deep dynamic stall phase with considerable flow unsteadiness. Figure 4 shows the pitching axis 0.25c downstream of the chord line's leading edge. As already mentioned, based on the chord length and freestream velocity, the Reynolds number is 2.4×10^6.

https://doi.org/10.1017/aer.2023.62 Published online by Cambridge University Press

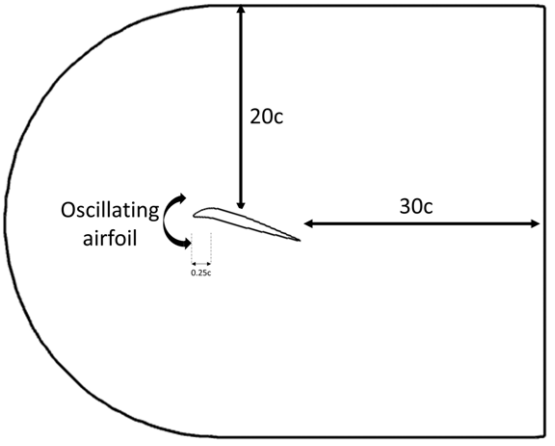

Figure 4. *Computational domain with the pitching mode.*

One of the most important aspects in numerical simulations is the discretisation of the computational domain. It is common practice to spend most of the time analysing and studying the grid generation in order to find a grid-independent solution: a good trade-off between accuracy and computational effort must be found, which is most often addressed by a trial-and-error approach in which the numerical solution is compared with experimental data or analytical solutions. The mesh sensitivity analysis conducted after the initial validation process is detailed in the next section. The selection of a correct size and shape for the computational domain are crucial factors for the results quality, and they are strongly dependent on the aerodynamic characteristics, and on the type of the problem which is faced.

A hybrid mesh made from a combination of structured and unstructured mesh was generated with ANSA, a multidisciplinary CAE pre-processor. It consists of a structured quadrilateral layer mesh around the aerofoil and an unstructured triangular mesh for the rest of the domain. Moreover, with the use of a blunt trailing edge it was possible to obtain O-shaped block layers around the aerofoil and most importantly, to prevent instabilities of the solution induced by singular points located at the sharp corners of the trailing edge.

Figure 5 models the simulation domain with two mesh regions: (i) the inner rotating grid, and (ii) the outer stationary grid. The total number of elements in the grid is 103,212, and the boundary region's first layer height is 0.006 mm with a bias factor of 1.08. The internal region has a minimum element length of 0.001 mm, a maximum length of 0.035 mm, and a bias factor of 1.08, while the external region has a minimum length of 0.035 mm, a maximum length of 0.6 mm and a bias factor of 1.08. The use of an internal circular domain allowed the mesh to move with the pitching aerofoil without affecting the simulation's cell quality. High-quality quadrangular elements were used to refine the grid for its numerical stability in simulations, and mesh-independent results were obtained. Sliding meshes were applied to the interfaces between the circular and external domains, thus designing non-matching nodes due to rotation, called 'hanging nodes': this improves the flow prediction near the walls. Since the nodes should have a constant position in their moving frame, no smoothing dynamic mesh approach was needed, and the quality remained the same.

The simulations were performed with a commercial CFD solver, called ANSYS Fluent. All scaled residuals were expected to decrease below $1x10^{6}$. The matching length of each time step was found to be below the sliding interface's minimum cell length to limit the interpolation error.

2.3 Validation of results

Figure 6(a) shows the aerofoils unsteady motion expressed by the lift coefficients variation with time for three pitching cycles and Fig. 6(b) shows the lift coefficient vs angle-of-attack for the same timescale.

https://doi.org/10.1017/aer.2023.62 Published online by Cambridge University Press

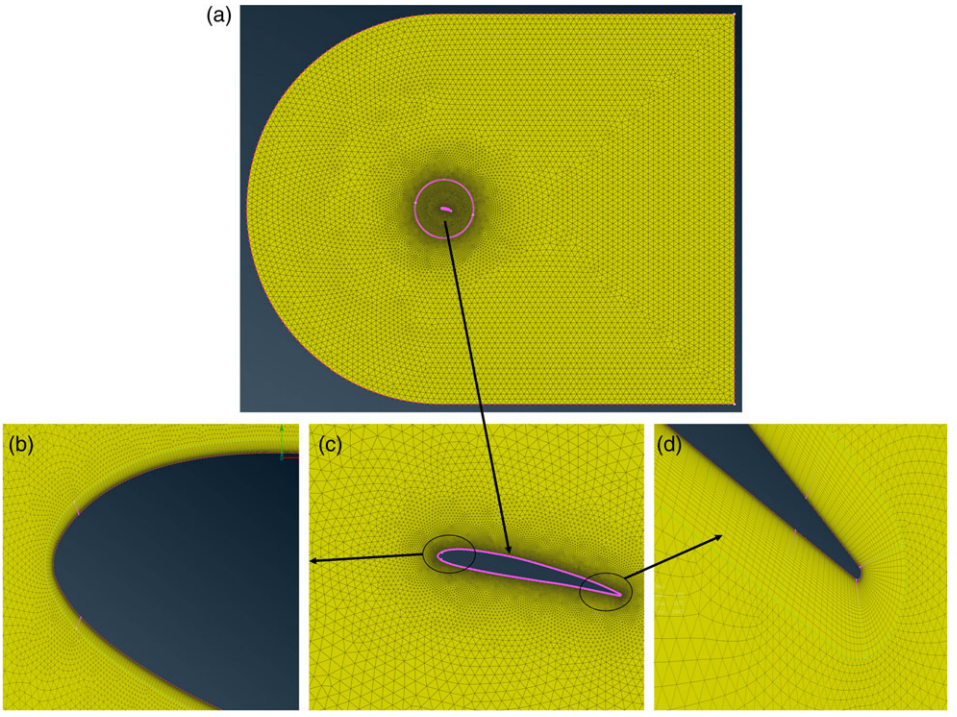

Figure 5. *Mesh structure around the aerofoil (a) mesh around the aerofoil; (b) near the leading-edge, (c) near the aerofoil, and (d) near the trailing-edge.*

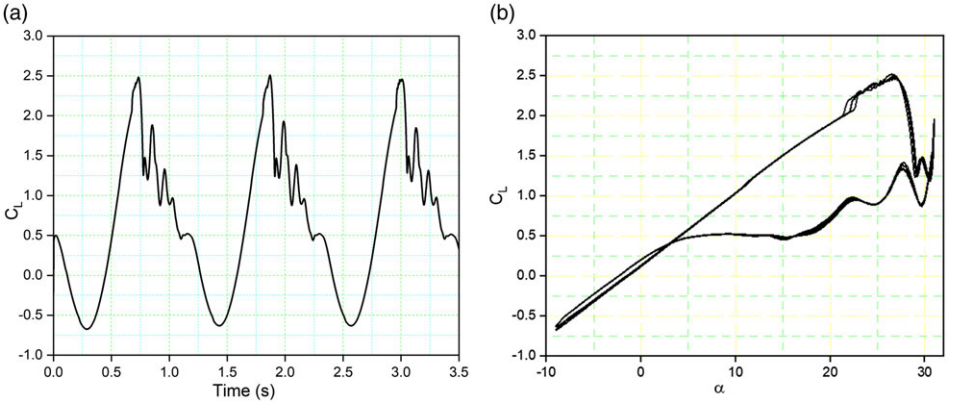

Figure 6. *Lift coefficient variation with time for the pitch oscillating aerofoil.*

As soon as the lift coefficient reaches its highest value, a sudden decrease is observed, thus depicting the beginning of the downstroke phase. The comparison of experimental with computational results was not close enough the due to large vortices on the aerofoil surface, that were predicted by the transition SST model and the flow three-dimensionality.

Table 1 presents the properties of three different grid sizes which have been used for grid independency investigations. Figure 7 shows the lift coefficient versus the angle-of-attack for these three different grid sizes. Good correlation between each hysteresis loop is shown and the upstroke and downstroke also showed a good agreement. The lift coefficients for grid size 1 and grid size 2 are slightly different in the

https://doi.org/10.1017/aer.2023.62 Published online by Cambridge University Press

Table 1. *Grid properties of the three grid sizes for the grid-sensitivity analysis*

Grid size	Number of cells	Min length	Max length	Bias factor
1	62,626	0.001	0.06	1.12
2	103,212	0.001	0.035	1.08
3	206,038	0.001	0.02	1.05

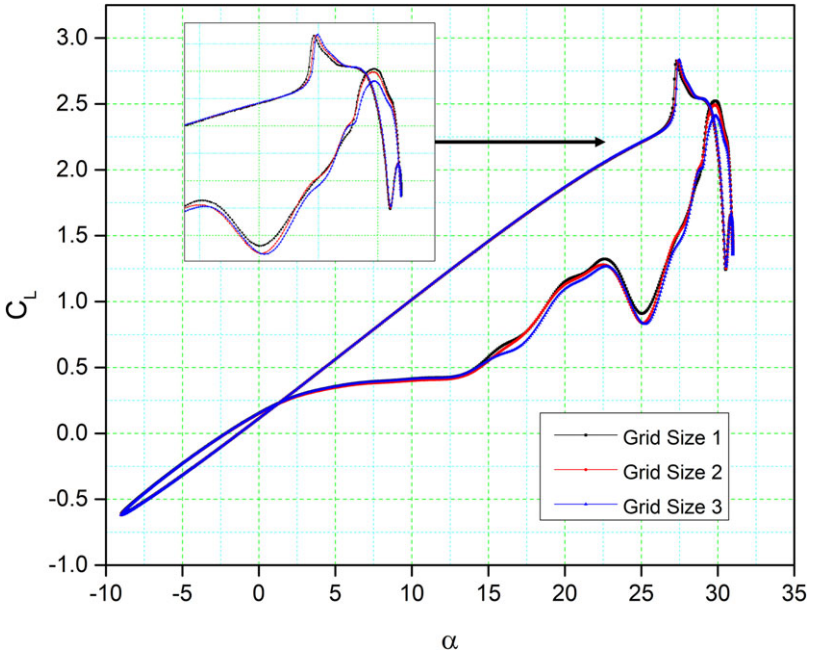

Figure 7. *Comparisons of the numerical results for the lift coefficient versus the angle-of-attack for three different grid sizes.*

down-stroke phase, and the stall (the peak of the lift curve) has a slight variation. Additionally, the fluctuations in the lift coefficient for all the three grid sizes are similar in shape and magnitude. Similarly, very small discrepancies are visualised between grid size 3 and the other two grid sizes during the upstroke, while a small difference can be seen between the lift coefficients in the downstroke. The flow reattachment location for all grid sizes is the same. Therefore, grid size 2 was selected as the computational domain due to acceptable (medium size) cell count and results obtained.

Figure 8 compares the model's computed lift and drag coefficients to their experimental values [81] and numerical data from previous literature [82]. The first simulation example used as a reference the experiments of McAlister et al. with Reynolds number 2.5 x10^6 and reduced frequency $k = 0.10$, from 5^0 to 25^0, with a mean incidence of 15^0, while the second simulation example used for benchmarking Correa et al.'s 2015 numerical data for the same settings.

The *SST* $k - \omega$ turbulence model can forecast the results' trend. The lift coefficient corresponds with its experimental value in the upstroke phase but it predicts the stall differently than the experimental results. As the unsteady analysis is often dissipative, it reduces the flow intensity and thus the kinetic energy. The numerical result is good, as it captures the load variation trend before the stall region. The ranges of differences in the peak noticed in the lift coefficient is small. The down-stroke variations are due to the extensive post-stall process, and hence discrepancy in the initial LEV prediction.

Figure 8(b) illustrates the drag coefficient variation with angle-of-attack and a difference exists particularly when $\alpha > 12$, as the deep stall causes the drag to increase. The drag coefficient with angle-of-attack

https://doi.org/10.1017/aer.2023.62 Published online by Cambridge University Press

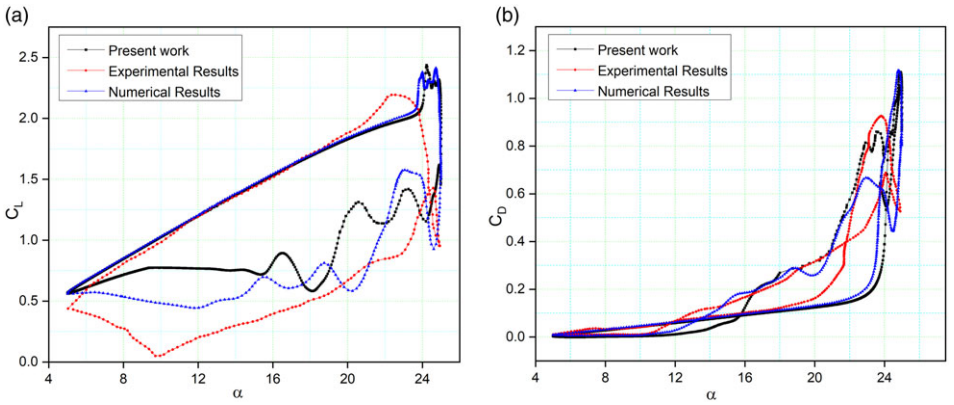

Figure 8. *Comparison of our numerical results with experimental results obtained from previous wind tunnel tests [65] and numerical results [66]: (a) lift coefficient; (b) drag coefficient.*

in Correa's numerical simulations is lower than the drag coefficient obtained in the other simulations. However, our numerical results of aerofoil's maximum drag coefficient are lower than the experimental results due to large vortices on the aerofoil surface and to the flow three dimensionality. These vortices occur because of the persistent flow separations at high angles of attack, which makes it difficult to effectively describe the viscous effects near the aerofoil surface. The CFD simulations in our study also indicate a secondary LEV that contributes to the recovery of the lift and drag coefficients around the maximum angle-of-attack.

3.0 Discussion of results

The outcomes of the optimisation procedure are expressed in terms of LE and MTE aerofoil designs in the first part of this section. The findings of the unsteady flow analysis are presented in the second part of this section in order to better understand the DSV studies and the results of various aerofoil configurations.

3.1 Optimisation results

The aerodynamic optimisation was obtained for the MLE and MTE aerofoils using the methodology presented in Ref. (7). The study presents the leading edge and trailing edge optimisation results of the S45 UAS' aerofoil and will demonstrate the overall benefits of the morphing.

Figure 9(a) indicates that the lift coefficients of the MLE aerofoil are higher than those of the reference aerofoil at Reynolds number $= 2.4 \times 10^6$, where C_L is 1.57 and 1.65 for the MLE and the reference aerofoil, respectively, thus representing a 5.09 % increase, and a static angle-of-attack increase of 3°. Figure 9(b) shows the lift-to-drag ratio of the reference aerofoil and the optimised aerofoils and reveals a 3.8 % increase for $\left(\frac{C_L}{C_D}\right)_{max}$ for MLE when compared to the reference aerofoil.

Figure 9(c) shows the pressure variations with the chord for MLE and reference aerofoils. The MLE aerofoil upper surface has the higher-pressure fluctuations than the reference aerofoil. The chord-wise pressure distribution shows that the MLE optimised aerofoil's cruise performance was improved by delaying the turbulent flow towards the trailing edge.

Figure 10(a) shows that the optimised aerofoil has higher lift coefficients than the reference aerofoil. The MTE lift coefficient was improved by maximum of 8.6% over the reference aerofoil. In addition, the MTE aerofoil stall angle increased by 2° with respect to the reference aerofoil stall angle.

https://doi.org/10.1017/aer.2023.62 Published online by Cambridge University Press

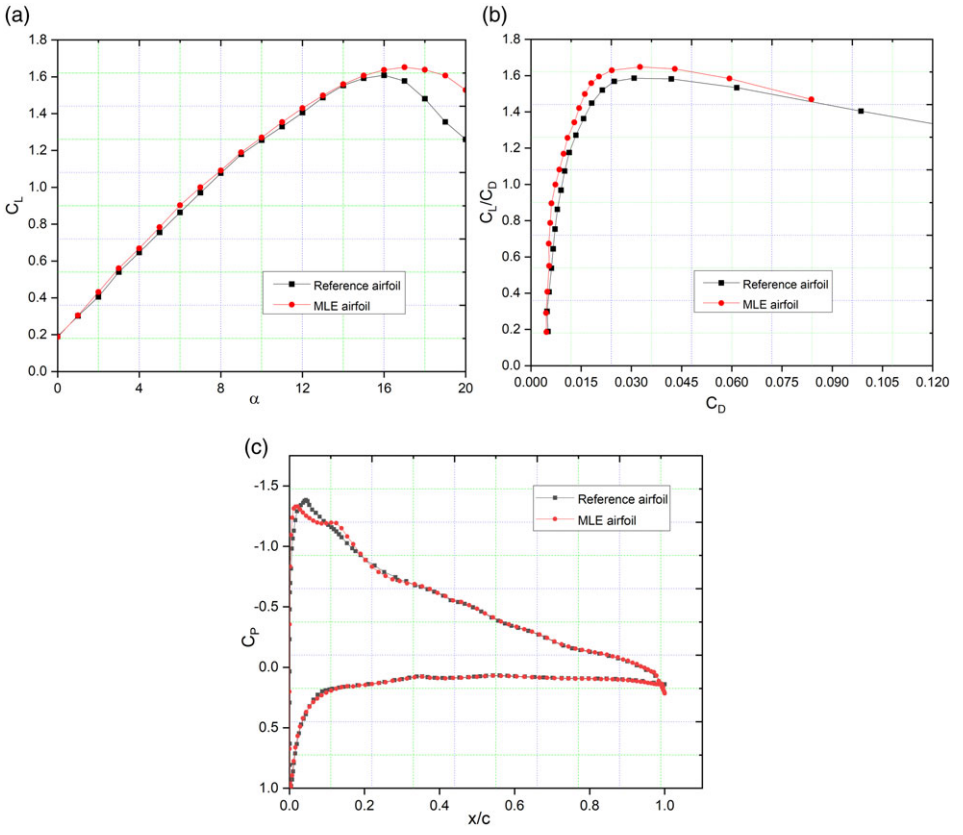

Figure 9. *Comparison of aerodynamic coefficients: (a) C_L, (b) C_L vs C_D ratio and (c) C_P of the MLE versus the reference aerofoil coefficients.*

Figure 10(b) shows the drag polar of the reference aerofoil, and the optimised MTE aerofoil. The morphing MTE aerofoil has a higher $\frac{C_L}{C_D}$ ratio than the reference aerofoil. Figure 10(c) shows the reference versus the MTE aerofoil pressure coefficients at 10° angle-of-attack. The MTE aerofoils have larger suction peaks than the reference aerofoil.

Figure 11 presents the velocity contour with streamlines depicting the separation bubble on the reference aerofoil at an angle-of-attack of 10°. The LSB can be seen over the leading edge of an aerofoil. The separation area was not visualised at lower angles of attack.

Figure 12 shows the aerofoil upper surface skin friction coefficient variation at angles of attack (AoA) of 2°, 6° and 10°. Figure 12(a) depicts the aerofoil lower surface skin friction coefficients by showing their way of increase with the incidence angle. The skin friction coefficient distribution on the upper surface of the aerofoil shows that the transition position moves towards the leading edge gradually with the increase of the angle-of-attack. The skin friction coefficient curve at $\alpha = 10°$ shows an irregular variation, which is a typical trend for cases when flow separation exists. Figure 12(b) shows the upper surface skin friction coefficients with their higher values at higher angles of attack by indicating the reduced shear velocity. In addition, the presence of flow separation is seen at 0.036c.

3.2 Unsteady aerodynamics results

Unsteady numerical simulations of a sinusoidally pitching UAS-S45 aerofoil and its morphing configurations will be studied. Aerofoil pitching occurs at the quarter chord position. To analyse the dynamic stall, we demonstrate the occurrence of LEVs over the UAS-S45 aerofoil for different morphing aerofoil

https://doi.org/10.1017/aer.2023.62 Published online by Cambridge University Press

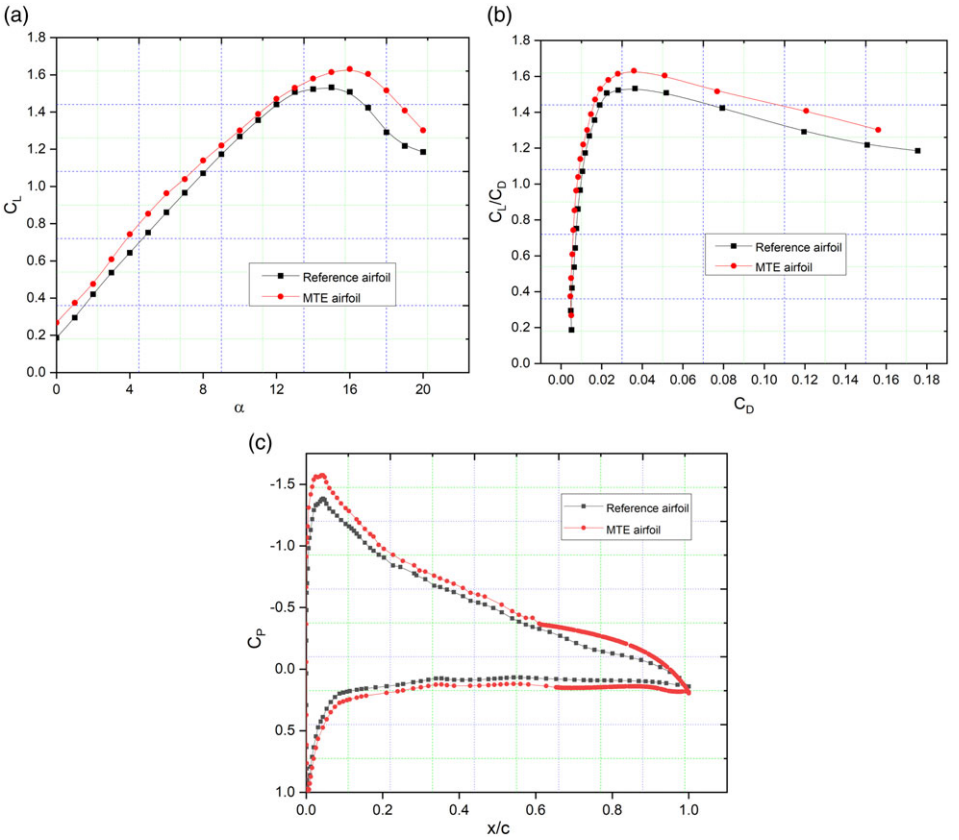

Figure 10. *Comparison of aerodynamic coefficients: (a) C_L, (b) C_L vs C_D ratio and (c) C_P of the MLE versus the reference aerofoil coefficients.*

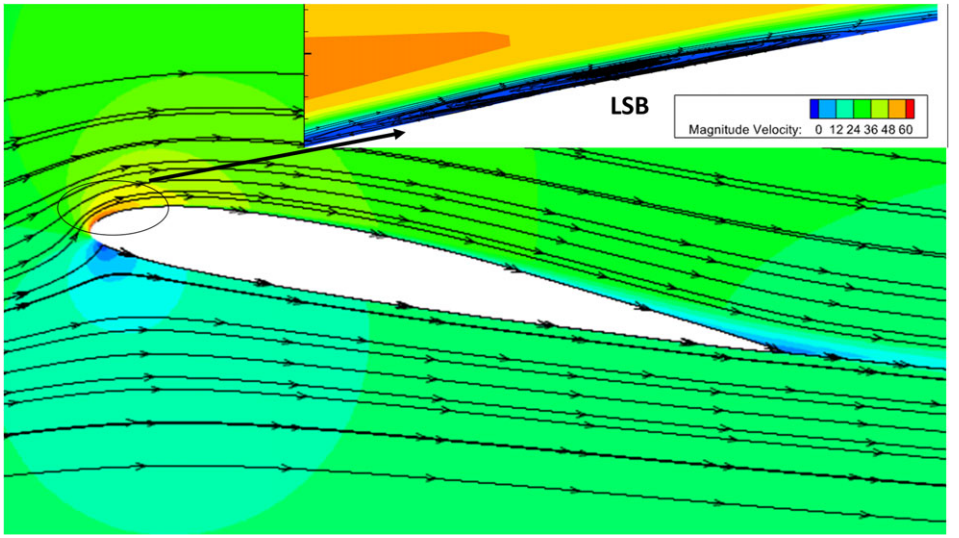

Figure 11. *Velocity contour with streamlines at an angle-of-attack of 10°.*

https://doi.org/10.1017/aer.2023.62 Published online by Cambridge University Press

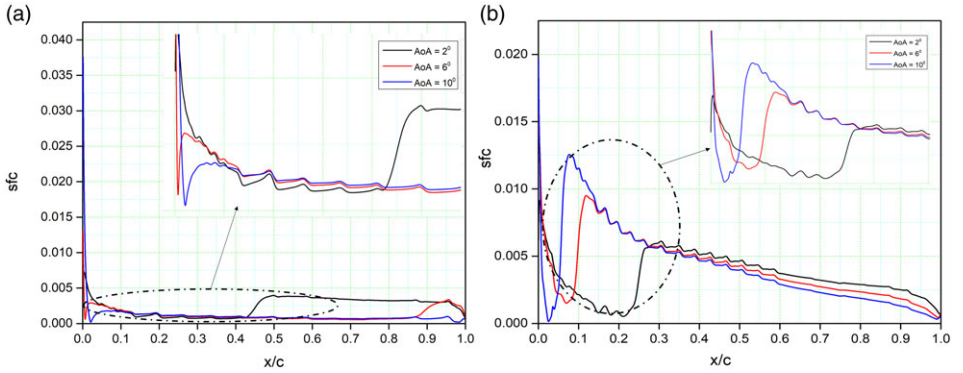

Figure 12. *Skin friction coefficient variation with the chord location on the: (a) upper surface and (b) lower surface.*

configurations. Using this unsteady flow phenomena over the optimized aerofoil configurations, the dynamic stall analysis will be presented.

3.2.1 Effect of reduced frequency on the UAS-S45 aerofoil

Figure 13 presents a comparison of aerodynamic coefficients at different reduced frequencies for $\alpha\,(t) = \alpha_m + \alpha_a \sin(\omega t)$. The effect of the reduced frequency on the unsteady pitching aerofoil motion is investigated by plotting the C_L versus the angle-of-attack for several reduced frequencies $k = 0.05$, 0.08, 0.12, 0.16, and 0.20 at $\mathrm{Re} = 2.4 \times 10^6$. As shown in Fig. 13, $C_{L,max}$ increases with the reduced frequency values; from $C_{L,max} = 2.43$at $k = 0.05$, $C_{L,max} = 2.49$at $k = 0.08$, $C_{L,max} = 2.54$ at $k = 0.12$, $C_{L,max} = 2.59$at $k = 0.16$ and 2.64 at $k = 0.20$. A greater k value broadens the hysteresis loops but does not affect the lift curve slope. Figure 13(b) shows a similar behaviour for the drag coefficient, but k has a mixed influence ($C_{D,max}$). That is, increasing k changes $C_{D,max}$ from 1.17 at $k = 0.05$ to 1.45 at $k = 0.2$. Table 2 clearly shows the values of $C_{L,max}$ and $C_{D,max}$. Different types of vortices are generated at the trailing edge, as it can be seen from the downstroke. These vortices increase the lift force from the instant in which they are produced until their separation and shedding into the downstream wake. This process continues until the vortices are no longer present.

The vortex patterns at various instances of a dynamic stall cycle for $k = 0.05$ case are shown in Fig. 14. Figure 14(a) depicts the upstroke LEVs in stall formation at four values of AoA. At $\alpha = 25.5°$, the formation of fully developed primary LEV is visualised, along with the beginning of a secondary LEV. This phenomena occurs as the incoming flow from the aerofoil above the stagnation point enters the vortex. The fluid bypasses the vortex and enters the boundary layer at the trailing edge. However, the primary vortex rolls up under the action of the secondary vortices, which enter in the boundary layer. As the angle-of-attack increases, more high-energy flow enters in the primary vortex, thus increasing its size. The separation point advances towards the trailing edge as the vortex increases. Secondary and tertiary vortices are visualised in the last two portions of Fig. 14(a).

At $\alpha = 27.3°$, the flow on the bottom of the aerofoil increases the size of the first trailing edge vortex. As the angle-of-attack increases to 28.8°, the separation point advances further behind the trailing edge, the mass of the fluid entering covers the entire aerofoil, and the lift coefficient reaches its maximum. A part of the fluid enters as upstream vortices along the boundary layer, while the rest of it is transported downstream into the wake. A secondary trailing edge vortex appears, and large vortices confirm the dynamic stall occurrence.

Figure 14(b) depicts the velocity contour in the downstroke phase. At $\alpha = 27.92°$, the separation points travel behind the trailing edge, a vortex structure covers the entire aerofoil from its leading edge to its trailing edge, and the lift coefficient increases. As the angle-of-attack reaches 20.42°, the bigger

https://doi.org/10.1017/aer.2023.62 Published online by Cambridge University Press

Table 2. *Aerofoil performance parameters at different reduced frequencies*

k	$C_{L,\,max}$	$\Delta C_{L,max}$	α_s [°]	$_{D,max}$	$\Delta C_{D,max}$
0.05	2.43	1.09	24.41	1.17	0.7
0.08	2.49	1.15	26.70	1.29	0.82
0.12	2.54	1.2	27.18	1.39	0.92
0.16	2.59	1.25	28.01	1.44	0.97
0.20	2.64	1.3	28.50	1.45	0.98

Note: $C_{L,\,max}$ = max dynamic lift coefficient; $C_{D,max}$ = max drag coefficient; α_{ds} = dynamic stall angle; $\Delta C_{L,max}$ = max lift difference from steady state results; $\Delta C_{D,max}$ = max drag coefficient difference from steady state results.

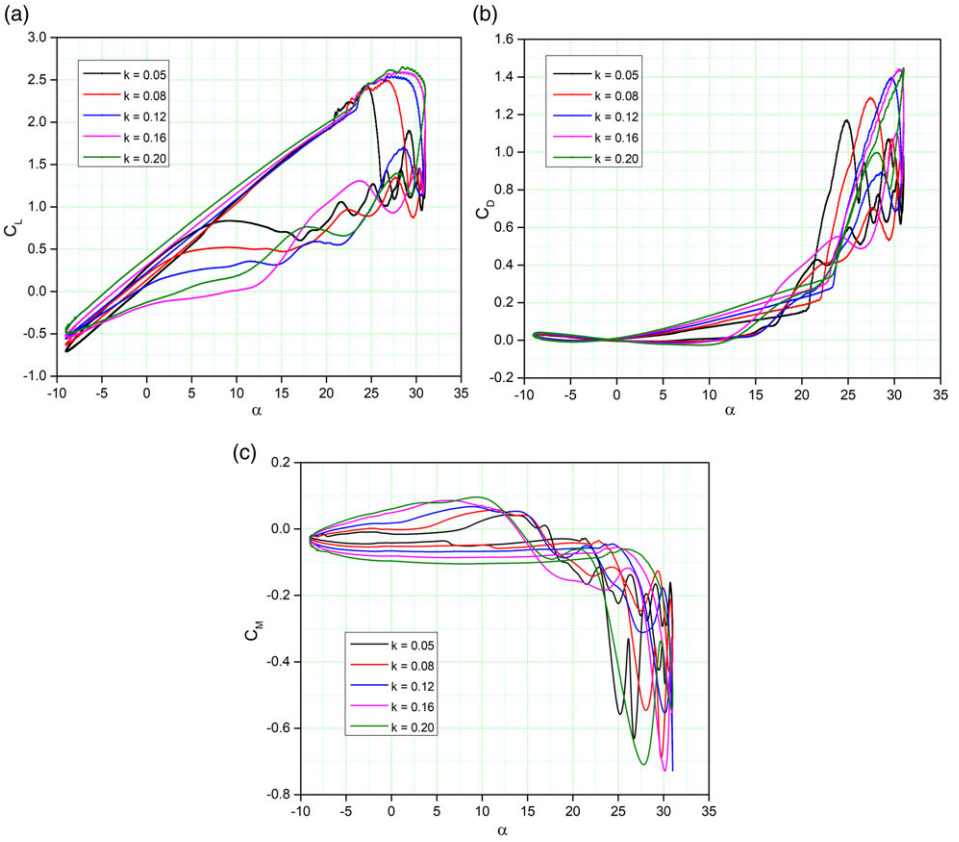

Figure 13. *Aerodynamic coefficient hysteresis loops at different reduced frequencies for the variations of the (a) lift coefficient, (b) drag coefficient, and (c) pitching moment coefficient with the AoA.*

vortex reduces and starts to merge into the flow. The separation points travel upstream, and these vortices disappear at 13.91°. The vortex region is sucked into the boundary layer, and a part of it is transferred downstream into the wake. Eventually, the separation zones disappear, and the reattached flow occurs at the low angles of attack.

Figure 15 reveals the stall development for up-stroke and down-stroke cycles of the aerofoil for a higher reduced frequency of $k = 0.16$. In Fig. 15(a), at upstroke angle-of-attack of 20.3°, the flow evolves slowly and stays attached to the aerofoil; the LSB is small and starts to form without a visible vortex. At 25.5°, the LEV evolves along the leading edge and continues to grow slowly. The increase of the angle-of-attack to 27.3° makes the LEV bigger and stronger. However, the dynamic stall can be seen at similar angles of attack, as it can be seen at $k = 0.05$ in Fig. 14(a).

https://doi.org/10.1017/aer.2023.62 Published online by Cambridge University Press

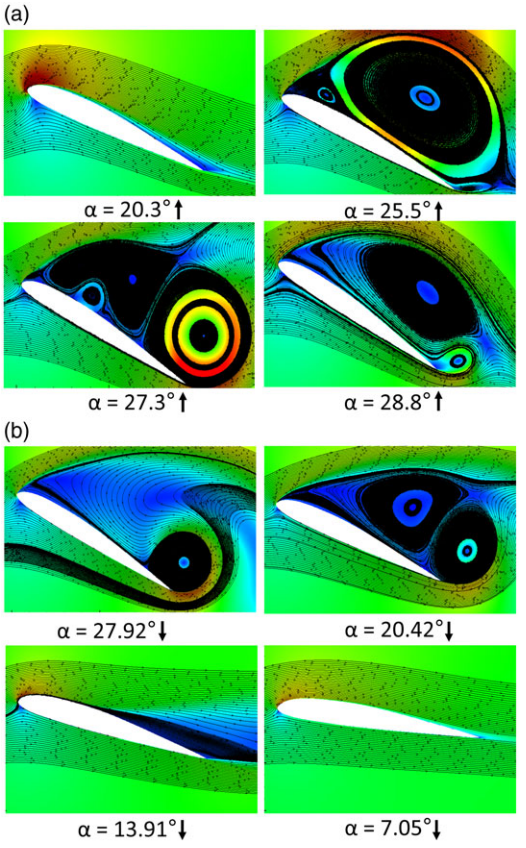

Figure 14. *Velocity contour superimposed with flow at $k = 0.05$: (a) up-stroke cycle and (b) down-stroke cycle.*

Figure 15(b) shows the downstroke flow angles; multiple vortices are located over the aerofoil at 27.92°, and the vortices merge and reduce in size at 20.42° and 13.91°. One important aspect is that the flow fails to fully reattach at higher reduced frequencies, which can also be seen in the downstroke cycle shown in Fig. 14(b).

Table 2 presents the results expressed in terms of aerodynamic parameters and stall features of an oscillating aerofoil at different reduced frequencies. The values of the stall angle-of-attack (α_{ds} [°]) reveal how reduced frequencies resulted in different dynamic stall angles. The stall angle increased from $k = 0.05$ to $k = 0.20$ by 4 degrees. It can be seen that the lift coefficient increases with the increasing reduced frequency. The lift coefficient of a pitching aerofoil is higher than that of a static aerofoil. Table 2 shows that the lift and drag coefficients variations during pitching motion at different reduced frequencies, and they increase at higher reduced frequencies.

3.2.2 Effect of the MLE

Figure 16 compares the aerodynamic coefficients of the morphing leading-edge aerofoils to those of a reference aerofoil with respect to the angle-of-attack over one complete cycle. Figure 16(a) shows that morphing aerofoils have both successfully increased $C_{L,max}$ value from 2.49 to 3.04. It is also clear that the morphing leading edge increased $C_{L,max}$, with the stall angle-of-attack increase. The main objective of the stall study is to delay or increase the stall angle, as stall angle-of-attack delay helps to maintain the aerofoil lift coefficient even in the downstroke cycle. However, this result indicates that a strong vortex has been formed in the leading-edge of aerofoil, which later results in dynamic stall.

https://doi.org/10.1017/aer.2023.62 Published online by Cambridge University Press

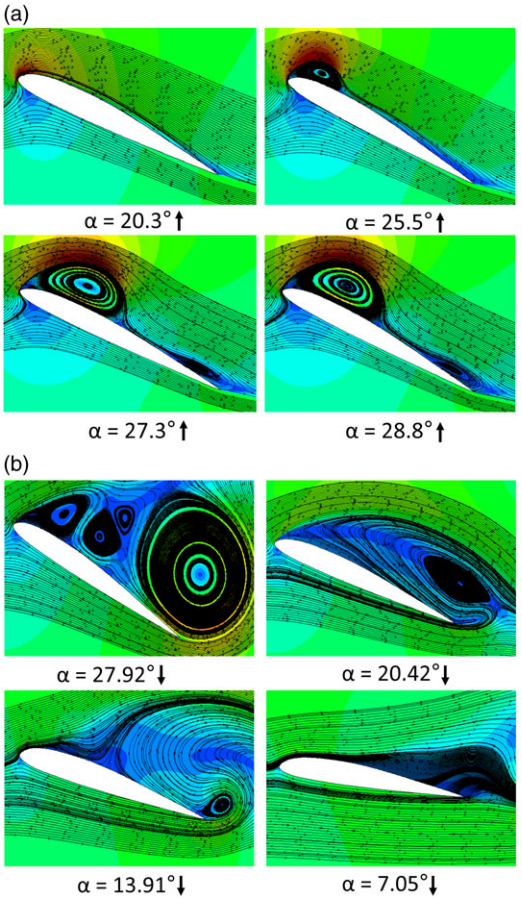

Figure 15. *Velocity contour superimposed with flow at k = 0.16: (a) up-stroke cycle and (b) down-stroke cycle.*

Similarly, the drag coefficients are lower for the MLE aerofoil for AoA lower than 30°, and the $C_{D,max}$ increases substantially at the peak angle with respect to the reference aerofoil, as seen in Fig. 16(b). Therefore, the drag coefficient of the MLE aerofoil remains low for a large range of angles of attack. The MLE aerofoil moment coefficient shows smaller C_M values with respect to those of the reference aerofoil, as seen in Fig. 16(c).

Figure 17(a) and (b) illustrate optimised MLE aerofoil streamlines and Mach number contours. Figure 17(a) depicts the flow development at different upstroke angles of attack for the reference aerofoil. The reference aerofoil's primary LEV can be clearly seen at 25.5° angle-of-attack. The clockwise vortex can also be seen near the trailing edge. As the angle-of-attack increases, the vortex size grows accordingly. The secondary and tertiary LEVs are also formed along with the primary LEV as the attack angle increases from 25.5° to 28.8°. The AoA increase results in more flow along the boundary layer by secondary and tertiary vortices, and a bigger trailing edge vortex at 29.8°and 31°.

In the case of an MLE aerofoil, as seen in Fig. 17(b), the flow separation phenomenon is slow at low angles of attack, such as 25.5°, as the flow remains largely attached to the aerofoil. By increasing the angle-of-attack to 28.8°, the leading-edge suction increases, and the LEV moves towards the trailing edge. The LEV also increases its size at 28.8°. This leading-edge vortex shedding is intensified by the formation of a small secondary vortex, which grows and breaks apart the main LEV. From 29.8° to 31°, the DSV is formed, which moves towards the trailing edge and increases the pitching moment coefficient.

https://doi.org/10.1017/aer.2023.62 Published online by Cambridge University Press

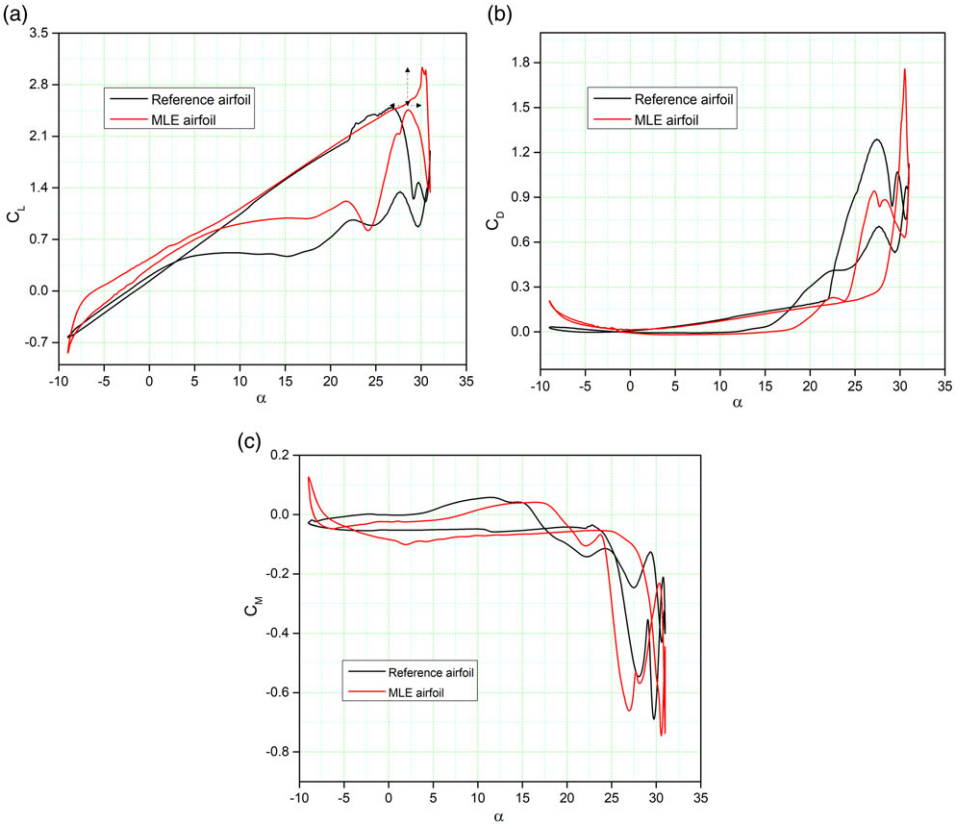

Figure 16. *Aerodynamic coefficient hysteresis loops at k = 0.08: (a) lift coefficient, (b) drag coefficient and (c) pitching moment coefficient.*

Large-scale vortical structures arise over the aerofoil in the separated zone during the up-stroke motion by causing a ripple in the surface pressure distribution at $\alpha = 25.5°$, as seen in Fig. 18(a). Figure 18(b) shows the separated flow impact on the skin friction coefficient at $x/c = 0.14$ at $\alpha = 25.5°$. The flow reattaches at $x/c = 0.24$, and it remains then in its attached state. The flow acceleration around the leading-edge increases as the aerofoil pitches up at $\alpha = 29.8°$, resulting in a larger peak suction and a stronger adverse pressure gradient across the laminar separation bubble. As shown in Fig. 18(c), the pressure coefficient is higher than -10 at $\alpha = 29.8°$, and the LEV formation can be clearly seen in the vicinity of the leading and trailing edges. The skin friction coefficients variations with the chord in Fig. 18(d) show that the flow separation is becoming bigger and is moving towards the trailing edge, accompanied by secondary and tertiary leading-edge vortices. The occurrence of the LEV is due to the increasing adverse pressure gradient, and then the dynamic stall vortex emerges and moves towards the trailing edge. As a result of the separation bubble occurrence, the skin friction coefficients show a large flow separation on the upper surface of the aerofoil. Figure 18(e) reveals that the negative pressure of the main vortex turns the flow from the pressure side of the aerofoil at the trailing edge towards the suction side by generating a counter-rotating trailing edge vortex. As depicted in Fig. 18(f), the leading-edge vortex continues to flow along the aerofoil surface by causing vortex shedding. Due to the shedding of the main leading-edge vortex, the lift coefficient begins to decrease.

Figure 19 illustrates the reference and optimised MLE aerofoils' vorticity contours during one pitching cycle. Figure 19(a) shows the boundary layer attached to a shear layer at an attack angle of 25.5°. As the oscillating aerofoil's angle-of-attack increases, reversed flow circulates from the trailing edge towards the leading edge ($\alpha = 29.8°$) as seen in Fig. 19(b). It shows a LEV that moves downstream

https://doi.org/10.1017/aer.2023.62 Published online by Cambridge University Press

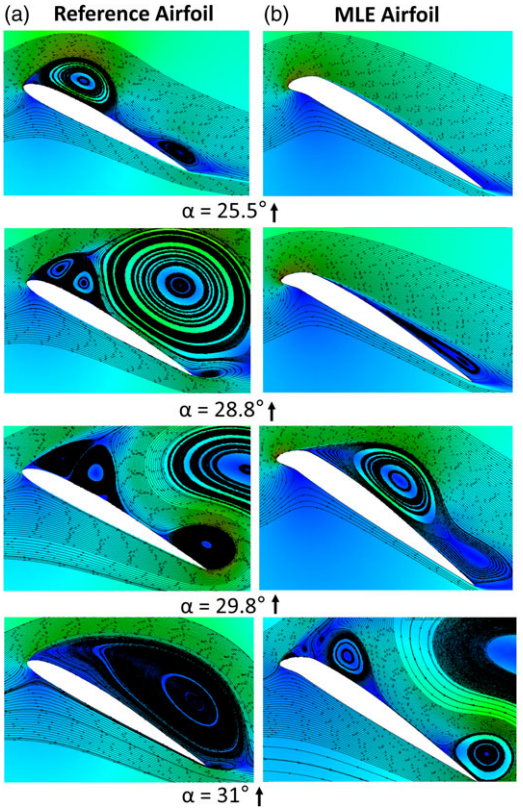

Figure 17. *Velocity contour superimposed with flow at different values of α: (a) reference aerofoil and (b) MLE aerofoil.*

along the aerofoil surface, and results in increased vorticity forces. The vorticity sheds away from the trailing edge at $\alpha = 30.8°$ shown in Fig. 19(c).

Figure 19(d) shows the MLE aerofoil's vorticity at an angle-of-attack of 25.5°. Figure 19(e) shows that the MLE aerofoils vorticity strength is less than the reference aerofoil at an angle-of-attack of 29.8°. At the same time, a strong TEV is produced during the stall at 30.8°: this vortex is quickly replaced by a secondary LEV that spans over the chord. Throughout the downstroke, alternating LEV and TEV creation and shedding causes force coefficient changes. The MLE aerofoil also stalls, but at a smaller AoA than the reference aerofoil.

Table 3 shows the maximum aerodynamic lift and drag coefficients, and their stall angle variations values of the reference aerofoil and of the MLE aerofoil. It is worth noting that the maximum lift coefficient increased by 22.08% and the maximum drag coefficient increased by 57.31% for the MLE aerofoil with respect to the to C_L of the reference aerofoil. An increased delay in the stall angle-of-attack of 14.26% was achieved with the optimised MLE aerofoil. Moreover, incremental values of $\Delta C_{L,max}$ and $\Delta C_{D,max}$ are provided for the MLE aerofoil with respect to the static aerofoil, in which the maximum lift coefficient of the MLE aerofoil increased by 47.82% with respect to the reference aerofoil maximum lift coefficient. The main objective of delaying the stall angle-of-attack was achieved, as it was delayed by 3.81° degrees.

3.2.3. Effect of the MTE

Figures 20(a) and (b) illustrate the velocity contours with streamlines of an optimised MTE aerofoil compared to those of the reference aerofoil. Figure 20(a) depicts the flow development over the reference

https://doi.org/10.1017/aer.2023.62 Published online by Cambridge University Press

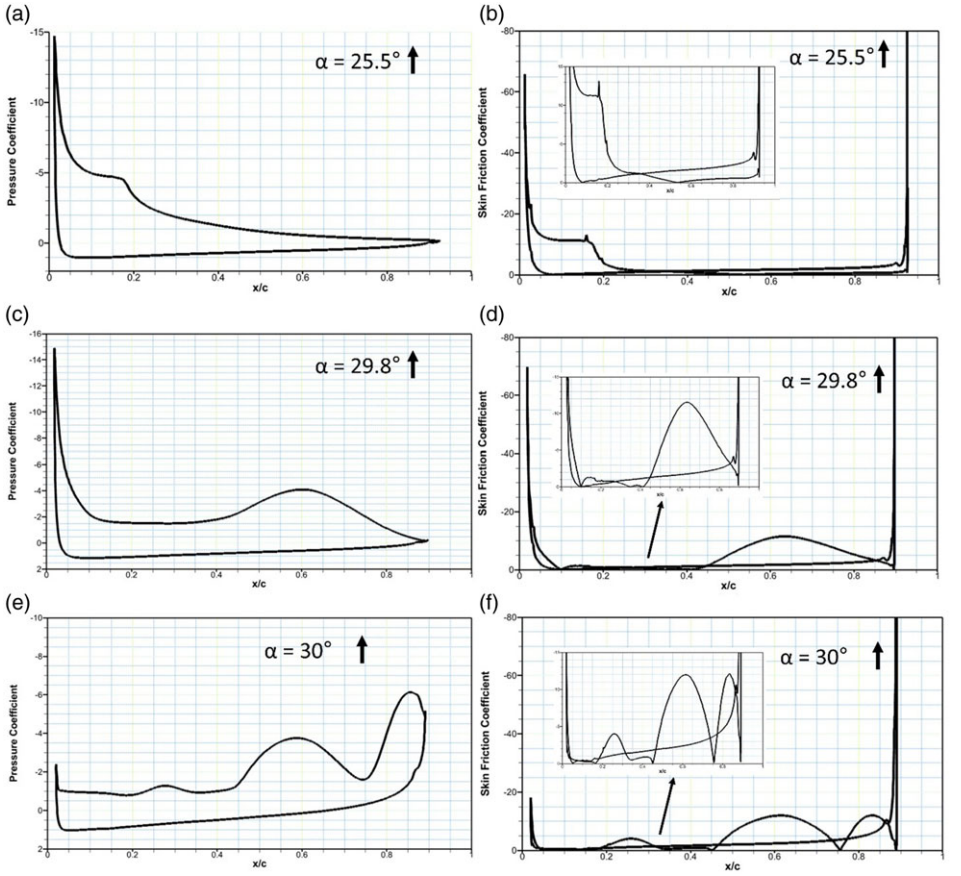

Figure 18. *Computed pressure and skin friction coefficients for a MLE aerofoil.*

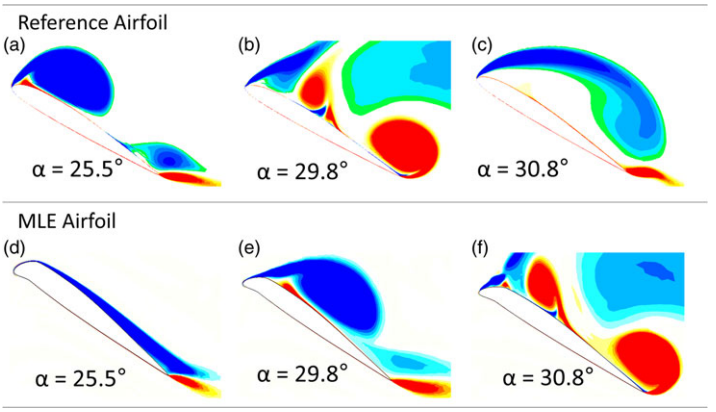

Figure 19. *Comparison of vorticity contours of the reference aerofoil with an MLE aerofoil at different angles of attack.*

aerofoil for different angles of attack. At $\alpha = 25.5°$, the flow remains attached to the aerofoil with a LEV. A small clockwise vortex can also be seen near the trailing edge. Subsequently, the secondary and tertiary LEVs are produced starting from the leading edge, and the primary vortex size increases significantly as the aerofoil pitches from 25.5° to 28.8°. The leading-edge suction results in the formation of a LEV

https://doi.org/10.1017/aer.2023.62 Published online by Cambridge University Press

Table 3. *Comparison of aerofoil performance parameters of the reference aerofoil with those of the MLE aerofoil*

Aerofoil	k	$C_{L,\ max}$	$\Delta C_{L,max}$	α_{ds} [°]	$C_{D,max}$	$\Delta C_{D,max}$
Reference	0.08	2.49	1.15	26.70	1.29	0.82
MLE	0.08	3.04	1.17	30.51	1.76	1.29

Note: $C_{L,\ x}$ = max dynamic lift coefficient; $C_{D,max}$ = max drag coefficient; α_{ds} = dynamic stall angle; $\Delta C_{L,max}$ = max lift difference from steady state results; $\Delta C_{D,max}$ = max drag coefficient difference from steady state results.

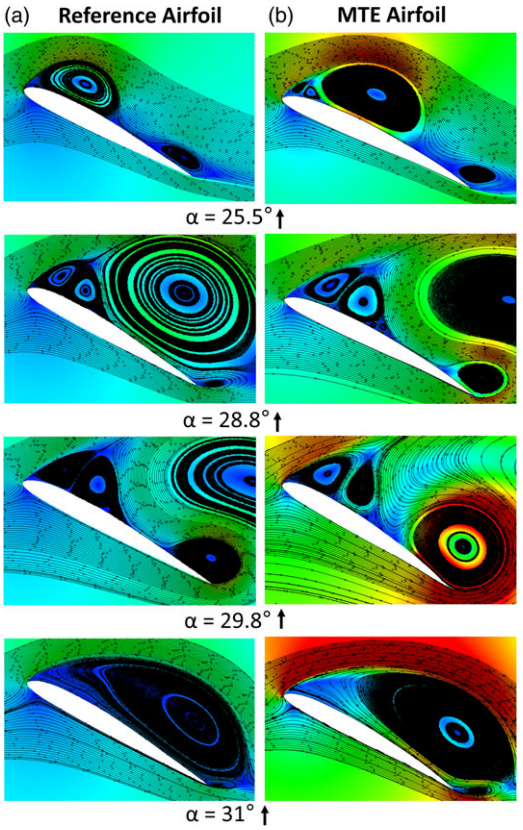

Figure 20. *Velocity contour superimposed with flow at different values of AoA for the (a) reference aerofoil and (b) MTE aerofoil.*

at 28.8°. This leading-edge vortex shedding is exacerbated by a tiny vortex formed at the leading edge, which increases from $\alpha = 29.8°$ and breaks from the main LEV. The LEV continues to increase and to spread over the aerofoil, as seen at the AoA of 31°.

Figure 20(b) shows that the MTE aerofoil at 25.5° has a small trailing edge separation area. As the angle-of-attack increases to 28.8°, the LEV increases and advances towards the trailing edge. Due to the growing pressure gradient at $\alpha = 29.8°$, the LEV bursts. It is evident that the trailing edge has resulted in an earlier stall formation than that of the reference aerofoil.

Figure 21 shows how a complete cycle of angles of attack impacts the aerodynamic coefficients of aerofoils equipped with a morphing trailing edge compared to the aerodynamic coefficients of the reference aerofoil. In Figure 21(a), the $C_{L,max}$ value increases from 2.49 to 2.67, while the morphing aerofoil shows C_L increase throughout the full angle-of-attack cycle with respect to the reference aerofoil. However, the stall angle-of-attack of MTE aerofoil is slightly lower than that of the reference aerofoil

https://doi.org/10.1017/aer.2023.62 Published online by Cambridge University Press

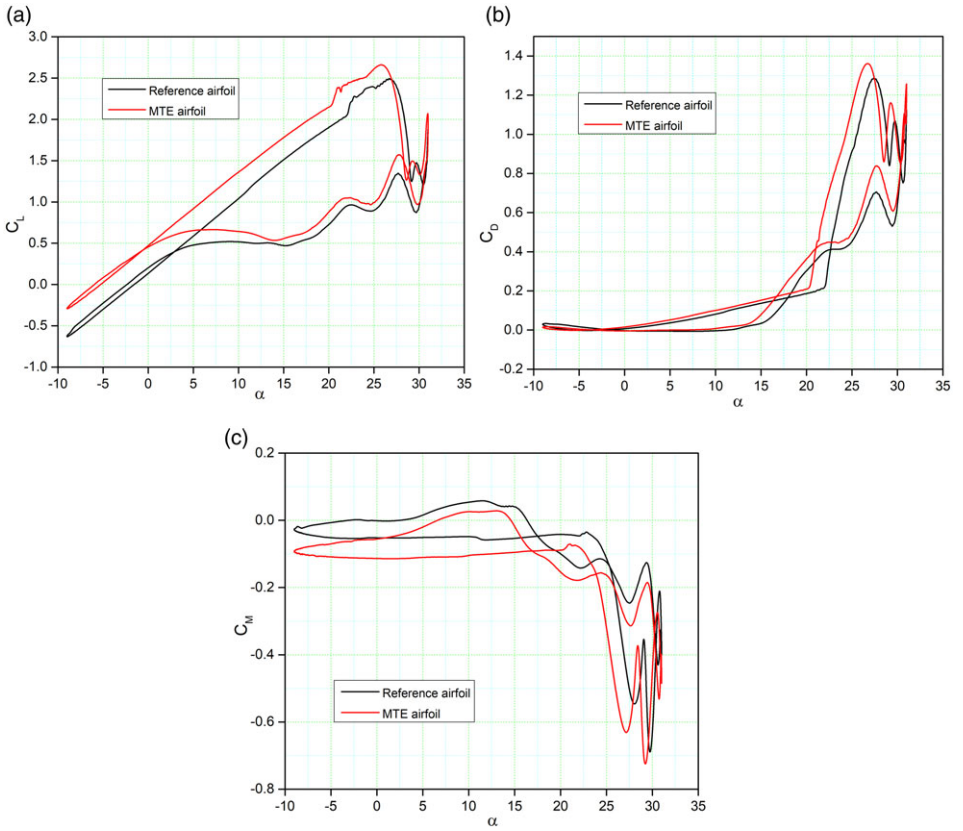

Figure 21. *Aerodynamic coefficient hysteresis loops at k = 0.08: (a) lift coefficient, (b) drag coefficient; (c) pitching moment coefficient.*

by 0.86°. The morphing aerofoil has a lift drop similar to that of the reference aerofoil during the down-stroke, as expected. Figure 21(b) and (c) display the coefficients of drag and moment, respectively, of the two aerofoils. Both $C_{D,max}$ and $C_{M,max}$ of the morphing aerofoil are higher than those of the reference aerofoil, with a maximum C_D increase of 5.42%.

Figure 22(a) shows the pressure coefficient variations with the chord position $\frac{x}{c}$ at the angle-of-attack of 25.5°, with only very large scale vortical structures growing over the aerofoil during up-stroke motion. This phenomenon results in smooth surface pressure contours. Figure 22(b) shows the occurrence of the separated flow on the skin friction coefficient at $\frac{x}{c} = 0.8$ for an angle-of-attack of 25.5°. When the angle-of-attack further increases to 29.8° (Fig. 22(c)), there is an increase in the leading-edge flow acceleration, resulting in a larger unfavourable pressure gradient, and resulting in a stall. Figure 22(c) shows the pressure coefficient at 29.8°, thus indicating that the pressure coefficient has a smaller value than −4 , and it clearly indicates that the LEV is at $x/c = 0.6$. Flow separation inflates and moves towards the trailing edge with many secondary and tertiary leading-edge vortices (see Figure 22(d)), and the bubble breaks down due to the increased adverse pressure gradient. The dynamic stall vortex is formed while moving towards the trailing edge. A significant separation of the skin friction coefficient is caused by the stall occurrence. The flow from the aerofoil's pressure side has a motion towards the suction side near the trailing edge, due to the negative pressure of the vortex causing a counter-rotating trailing edge vortex, as shown in Fig. 22(e) for the angle-of-attack of 30°. Figure 22(f) shows vortex shedding as the leading-edge vortex moves over the aerofoil surface. The leading-edge vortex dissipation causes a lift coefficient decrease.

https://doi.org/10.1017/aer.2023.62 Published online by Cambridge University Press

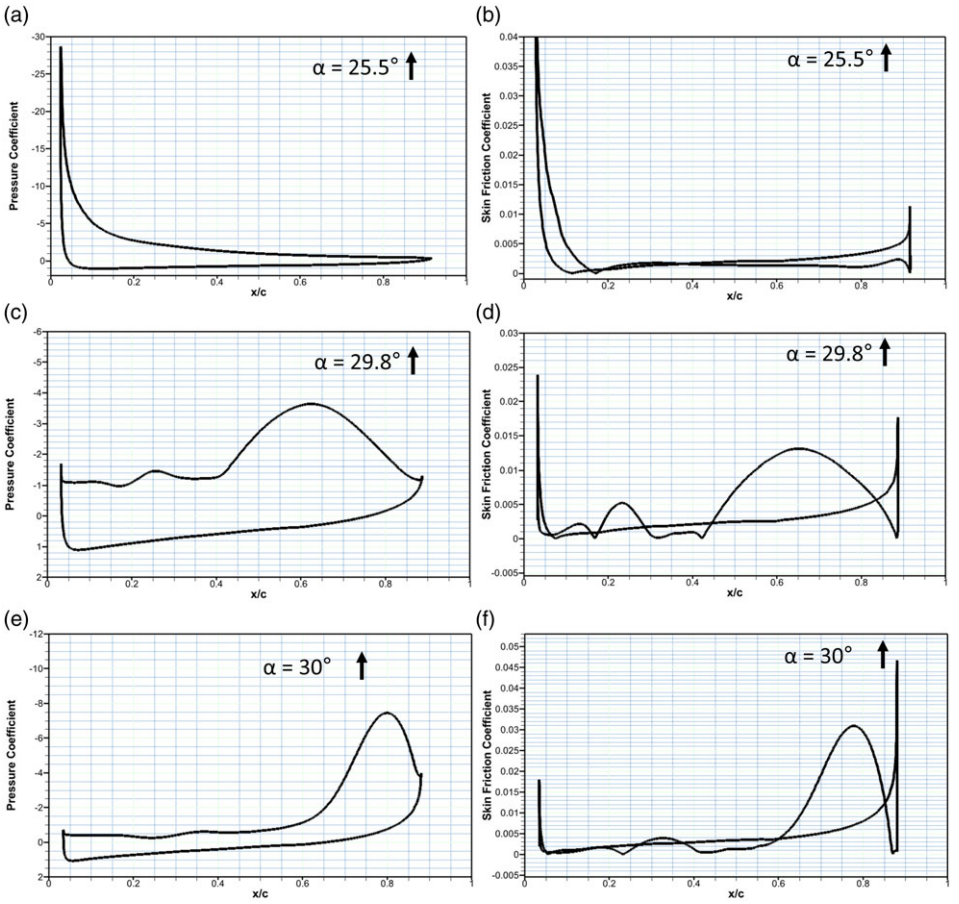

Figure 22. *Computed pressure coefficient and skin friction coefficient for the MTE aerofoil.*

Figure 23 shows the vorticity contours at different angles of attack during a pitching cycle for both the reference and the MTE aerofoils. Figure 23(a) and (d) reveal that the boundary layer separation takes place, and that the separation is more deepened for the MTE aerofoil. The flow remains attached to the rest of the aerofoil at angle-of-attack of 25.5°. When the angle-of-attack increases while the aerofoil oscillates, a more reversed flow area occurs in the MTE aerofoil than the reference aerofoil, moving from the trailing edge towards the leading edge as visualised at $\alpha = 29.8°$.

LEVs containing significant energy are created, and they migrate downstream on the aerofoil surface, as seen in Fig. 23(b), thus resulting in strong integral forces. These vortices structures are characterised by a stronger force coefficient curve slope, as displayed earlier in Fig. 13.

The MTE aerofoil also results in a much stronger vortex, as shown in Fig. 23(e), while a weaker TEV is produced at the critical angle-of-attack of 30.8° on the reference aerofoil, as shown in Fig. 23(c). This TEV dissipates downstream where it is replaced by a secondary LEV, which spreads over most of the aerofoil's chord span. Both LEVs and TEVs form and shed during the downstroke, causing significant force coefficient fluctuations. Using an MTE, the aerofoil fully stalled and with a higher strength than the one observed in the reference aerofoil.

Table 4 presents the aerodynamic coefficients and stall characteristics of the reference aerofoil and the MTE aerofoil. The stall angle-of-attack was increased by1° for the MTE aerofoil with respect to that of the reference aerofoil. The maximum lift coefficient increased slightly by a maximum of 6.8%, and the maximum drag coefficient by 8.5%. The other results followed a similar trend, including the increase in maximum lift coefficient values of a pitching aerofoil compared to a static aerofoil.

https://doi.org/10.1017/aer.2023.62 Published online by Cambridge University Press

Table 4. *Comparison of aerofoil performance parameters of the reference aerofoil with the MTE aerofoil*

Aerofoil	k	$C_{L,\ max}$	$\Delta C_{L,max}$	α_{ds} [°]	$C_{D,max}$	$\Delta C_{D,max}$
Reference	0.08	2.49	1.15	26.70	1.29	0.82
MTE	0.08	2.67	1.32	25.84	1.36	0.89

Note: $C_{L,\ max}$= max dynamic lift coefficient; $C_{D,max}$ = max drag coefficient; α_{ds} = dynamic stall angle; $\Delta C_{L,max}$ = max lift difference from steady state results; $\Delta C_{D,max}$= max drag coefficient difference from steady state results.

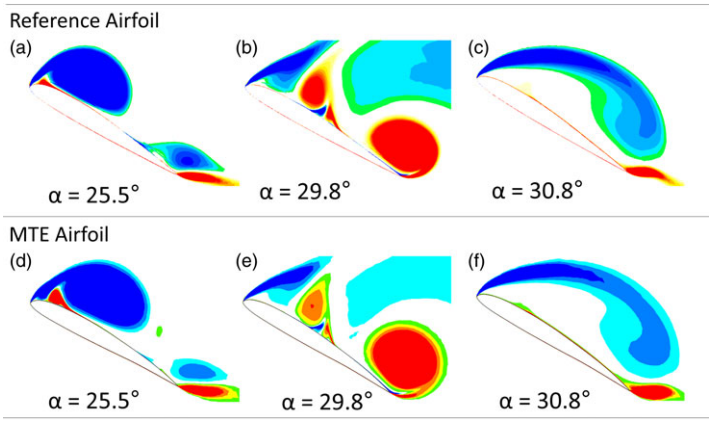

Figure 23. *Comparison of vorticity contours of the reference aerofoil with those of the MTE aerofoil at different angles of attack.*

4.0 Conclusion

This paper investigated the effect of the optimised MLE and MTE on the DSV around a pitching aerofoil through numerical simulations. Firstly, the optimisation of the UAS-S45 aerofoil was performed using a morphing optimisation framework. This framework used Bezier-PARSEC parametrisation and the PSO coupled with the PS algorithm with the aim of designing an aerodynamically efficient S-45 aerofoil. The $\gamma - Re_\theta$ transition turbulence model was applied to predict the laminar-turbulent flow transition region. Secondly, the study presented the unsteady analysis of the UAS-S45 aerofoil and its morphing configurations. Finally, the unsteady flow field and the aerodynamic forces were analysed at the Reynolds number of 2.4×10^6, and five different reduced frequencies. The lift (C_L), drag (C_D) and moment (C_M) coefficients of the reference and the morphing aerofoils were compared. Based on this study, the following conclusions were drawn:

The morphing aerofoils improved the overall aerodynamic performance and delayed the boundary layer separation. The lift coefficients of the MLE aerofoil compared to those of the reference aerofoil have higher values, increasing from 1.57 to 1.65, which represented a 5.09% gain, while the static angle-of-attack increased, by 3°. An increase of 3.8% in the maximum $\frac{C_L}{C_D}$ was obtained for an MLE aerofoil compared to the reference aerofoil.

- The optimal shapes of MTE aerofoil produced an increase of the lift coefficient with respect to the reference aerofoil of up to almost 8.6%. In addition, an increase of 2° in the static stall angle was obtained for the MTE aerofoil.
- The effect of the reduced frequency on the unsteady pitching motion was investigated by plotting the C_l versus the angle-of-attack for several reduced frequencies of $k = 0.05$, 0.08, 0.12, 0.16 and 0.20 at $\mathrm{Re} = 2.4 \times 10^6$. The $C_{L,max}$ increased with reduced frequency, from $C_{L,max}$= 2.43 at $k = 0.05$ to $C_{L,max}$= 2.64 at $k = 0.12$.

https://doi.org/10.1017/aer.2023.62 Published online by Cambridge University Press

- The results showed a similar pattern for the drag coefficients values; however, 'k' had a mixed effect on the maximum drag coefficients ($C_{D,max}$). $C_{D,max}$ changed from 1.17 at $k = 0.05$ to 1.45 at $k = 0.2$ and from $C_{D,max}$ of 1.29 at $k = 0.08$ to 1.44 at $k = 0.16$ as 'k' increased. On the downstroke, numerous sorts of vortices were formed near the trailing edge. From the time of their separation and shedding into the downstream wake, these vortices increased the lift force.
- It was found that higher reduced frequency stabilised the LEV that provided its lift by reducing lift variation during the dynamic stall phase. High-reduced frequency LEV stabilised the flow even when the aerofoil was in the downstroke. The $C_{L,max}$, $C_{D,max}$ and stall angles of attack were calculated for all reduced frequencies.
- The numerical results have shown that the new radius of curvature of the MLE aerofoil can minimise the streamwise adverse pressure gradient and prevent significant flow separation by delaying the DSV occurrence. Furthermore, it was shown that the morphing aerofoil delayed the stall angle-of-attack with respect to the stall of the reference aerofoil by 14.26 %, and $C_{L,max}$ of the aerofoil increased from 2.49 to 3.04.
- However, while the MTE aerofoil was found to increase the overall lift coefficient and the $C_{l,max}$, it did not affect the dynamic stall. Vorticity behaviour during DSV generation and separation has shown that the MTE can change vortices' evolution and increase vorticity strength from the leading-edge shear layer by increasing DSV flow.

To cause the wing to create the desired elastic deformation and to control the aircraft's stall, it depends on the smooth deflection of leading anad trailing edge control surfaces. However, according to the analysis of the flexible wing's aerodynamic properties, the control efficiency of the wings' leading and trailing edges becomes complex as the speed increases. The resultant aerodynamic forces increase non-linearly with the control deflection. Therefore, it is significant to employ the appropriate control approach due to the control reverse effect phenomena brought on by the wing's flexibility.

A control allocation technique should be proposed to solve the leading and trailing edges multi-control surfaces deflection problem, specifying maximisation of the control effectiveness of the control surfaces. Several actuation mechanisms, such as smart material-based shape-memory alloy actuators or electromechanical actuator systems, can be implemented into the wing.

Additionally, Finite Element Analysis (FEA) should be performed to evaluate the structural advantages that actuation could provide, such as the ability to control the spanwise load. The requirements for more degrees of freedom, smooth transition with resonance frequencies, mode shapes, modal damping, etc., will provide detailed results for selecting proper actuation mechanisms.

Regarding future works, the LARCASE's Price-Padoussis subsonic wind tunnel will be used for wind tunnel studies of the MLE and MTE aerofoils. The findings are expected to clarify the flow physics and validate the results of the morphing aerofoil flow phenomena. In addition, we will use an optimised mathematical model that can govern the pitching motion (reduced frequency) along with the aerofoil deflection (deflection frequency) and the morphing starting time.

Acknowledgments. Special thanks are dues to the Natural Sciences and Engineering Research Council of Canada (NSERC) for the Canada Research Chair Tier 1 in Aircraft Modelling and Simulation Technologies grant. We would also like to thank Mrs. Odette Lacasse for her support at the ETS, as well as Hydra Technologies' team members Mr. Carlos Ruiz, Mr. Eduardo Yakin and Mr. Alvaro Gutierrez Prado in Mexico. We would like to thank the NSERC and Prof. Jeremy Laliberte for their support within the CREATE-UTILI program.

References

[1] ICAO. Aviation's contribution to climate change, Environmental report. *International Civil Aviation Organisation*, 2019.
[2] Frota, J. NACRE novel aircraft concepts, *Aeronaut. J.* 2010, **114**, pp 399–404.
[3] Kintscher, M., Wiedemann, M., Monner, H.P., Heintze, O. and Kühn, T. Design of a smart leading edge device for low speed wind tunnel tests in the European project SADE. International Journal of Structural Integrity, 2011.
[4] Papadopoulos, M. *Smart Intelligent Aircraft Structures (SARISTU)*; Springer-Verlag Berlin Heidelberg, 2016.

https://doi.org/10.1017/aer.2023.62 Published online by Cambridge University Press

[5] Botez, R. Morphing wing, UAV and aircraft multidisciplinary studies at the Laboratory of Applied Research in Active Controls, Avionics and AeroServoElasticity LARCASE. *Aerospace Lab*, 2018, pp 1–11.
[6] Hamy, A., Murrieta-Mendoza, A. and Botez, R. Flight trajectory optimization to reduce fuel burn and polluting emissions using a performance database and ant colony optimization algorithm, 2016.
[7] Bashir, M., Longtin-Martel, S., Botez, R.M. and Wong, T. Aerodynamic design optimization of a morphing leading edge and trailing edge airfoil–application on the uas-s45, *Appl. Sci.*, 2021, **11**, p 1664.
[8] Botez, R., Koreanschi, A., Gabor, O., Tondji, Y., Guezguez, M., Kammegne, J., Grigorie, L., Sandu, D., Mebarki, Y. and Mamou, M. Numerical and experimental transition results evaluation for a morphing wing and aileron system. *Aeronaut. J.*, 2018, **122**, pp 747–784.
[9] Botez, R.M. Overview of morphing aircraft and unmanned aerial systems methodologies and results–application on the cessna citation X, CRJ-700, UAS-S4 and UAS-S45. In *Proceedings of the AIAA SCITECH 2022 Forum*, 2022, p 1038.
[10] Botez, R.M., Molaret, P. and Laurendeau, E. Laminar flow control on a research wing project presentation covering a three year period. In *Proceedings of the Canadian Aeronautics and Space Institute Annual General Meeting*, 2007.
[11] Communier, D., Botez, R.M. and Wong, T. Design and validation of a new morphing camber system by testing in the price—Païdoussis subsonic wind tunnel, *Aerospace*, 2020, **7**, p 23.
[12] Murrieta Mendoza, A., Botez, R.M., Vucinic, D., Rodrigues Leta, F. and Janardhanan, S. Commercial aircraft trajectory optimization to reduce flight costs and pollution, 2019.
[13] Viviani, P., Aldinucci, M., d'Ippolito, R., Lemeire, J., Vucinic, D. A flexible numerical framework for engineering—A response surface modelling application, *Improv. Perform. Mater. Des. Exp. Approach.*, 2018, pp 93–106.
[14] Arena, M., Chiatto, M., Amoroso, F., Pecora, R. and de Luca, L. Feasibility studies for the installation of Plasma Synthetic Jet Actuators on the skin of a morphing wing flap. In *Proceedings of the Active and Passive Smart Structures and Integrated Systems XII*, 2018, pp 131–139.
[15] Dimino, I., Lecce, L. and Pecora, R. *Morphing Wing Technologies: Large Commercial Aircraft and Civil Helicopters*. Butterworth-Heinemann, 2017.
[16] Dimino, I., Pecora, R. and Arena, M. Aircraft morphing systems: elasticity of selected components and modelling issues. In *Proceedings of the Active and Passive Smart Structures and Integrated Systems IX*, 2020, p 113760M.
[17] Pecora, R. Morphing wing flaps for large civil aircraft: Evolution of a smart technology across the Clean Sky program, *Chin. J. Aeronaut.*, 2021, **34**, pp 13–28.
[18] Arena, M., Amoroso, F., Pecora, R., Amendola, G. and Dimino, I. Numerical and experimental validation of a full scale servo-actuated morphing aileron model, *Smart Mater. Struct.*, 2018, **27**, p 105034.
[19] Barbarino, S., Pecora, R., Lecce, L., Concilio, A., Ameduri, S. and De Rosa, L. Airfoil structural morphing based on SMA actuator series: numerical and experimental studies, *J. Intell. Mater. Syst. Struct.,* 2011, **22**, pp 987–1004.
[20] Ameduri, S., Concilio, A., Dimino, I., Pecora, R. and Ricci, S. AIRGREEN2-clean sky 2 programme: Adaptive Wing technology maturation, challenges and perspectives, *Smart Mater. Adapt. Struct. Intell. Syst.*, 2018, **51944**, p V001T004A023.
[21] Li, Y., Wang, X. and Zhang, D. Control strategies for aircraft airframe noise reduction, *Chin. J. Aeronaut.*, 2013, **26**, pp 249–260.
[22] Abbas, A., De Vicente, J. and Valero, E. Aerodynamic technologies to improve aircraft performance, *Aerosp. Sci. Technol.*, 2013, **28**, pp 100–132.
[23] Giuliani, M., Dimino, I., Ameduri, S., Pecora, R. and Concilio, A. Status and perspectives of commercial aircraft morphing, *Biomimetics*, 2022, **7**, p 11.
[24] Concilio, A., Dimino, I. and Pecora, R. SARISTU: Adaptive Trailing Edge Device (ATED) design process review, *Chin. J. Aeronaut.*, 2021, **34**, pp 187–210.
[25] Carossa, G.M., Ricci, S., De Gaspari, A., Liauzun, C., Dumont, A. and Steinbuch, M. Adaptive trailing edge: specifications, aerodynamics, and exploitation, In *Proceedings of the Smart Intelligent Aircraft Structures (SARISTU) Proceedings of the Final Project Conference*, 2016, pp 143–158.
[26] Liauzun, C., Le Bihan, D., David, J.-M., Joly, D. and Paluch, B. Study of morphing winglet concepts aimed at improving load control and the aeroelastic behavior of civil transport aircraft, *Aerospace Lab*, 2018, pp 1–15.
[27] Lepage, A., Amosse, Y., Brazier, J.-P., Forte, M., Vermeersch, O., and Liauzun, C. Experimental investigation of the laminar–Turbulent transition and crossflow instability of an oscillating airfoil in low speed flow. In *Proceedings of the IFASD 2019*, 2019.
[28] Sinapius, M., Monner, H.P., Kintscher, M. and Riemenschneider, J. DLR's morphing wing activities within the European network, *Procedia Iutam*, 2014, **10**, pp 416–426.
[29] Gabor, O.Ş., Simon, A., Koreanschi, A. and Botez, R. Application of a morphing wing technology on hydra technologies unmanned aerial system UAS-S4. In *Proceedings of the ASME International Mechanical Engineering Congress and Exposition*, 2014, p V001T001A037.
[30] Vu, P., Kelkar, A. and Whitmer, C. Investigation of the effects of stiffness on control power via a morphing wing technology. In *Proceedings of the 46th AIAA/ASME/ASCE/AHS/ASC Structures, Structural Dynamics and Materials Conference*, 2005, p 2039.
[31] Mathisen, S., Gryte, K., Gros, S. and Johansen, T.A. Precision deep-stall landing of fixed-wing UAVs using nonlinear model predictive control, *J. Intell. Robot. Syst.*, 2021, **101**, pp 1–15.
[32] Sekimoto, S., Kato, H., Fujii, K. and Yoneda, H. In-flight demonstration of stall improvement using a plasma actuator for a small unmanned aerial vehicle, *Aerospace*, 2022, **9**, p 144.
[33] Liiva, J. Unsteady aerodynamic and stall effects on helicopter rotor blade airfoil sections, *J. Aircr.*, 1969, **6**, pp 46–51.
[34] Richez, F. Analysis of dynamic stall mechanisms in helicopter rotor environment, *J. Am. Helicopter Soc.*, 2018, **63**, pp 1–11.

https://doi.org/10.1017/aer.2023.62 Published online by Cambridge University Press

[35] Larsen, J.W., Nielsen, S.R. and Krenk, S. Dynamic stall model for wind turbine airfoils, *J. Fluids Struct.*, 2007, **23**, pp 959–982.
[36] Zhu, C., Qiu, Y., and Wang, T. Dynamic stall of the wind turbine airfoil and blade undergoing pitch oscillations: A comparative study, *Energy*, 2021, **222**, p 120004.
[37] Brandon, J.M. Dynamic stall effects and applications to high performance aircraft, *Aircr. Dynam. High Angles Attack: Exp. Model.*, 1991.
[38] Nguyen, D.H., Lowenberg, M.H. and Neild, S.A. Analysing dynamic deep stall recovery using a nonlinear frequency approach, *Nonlinear Dyn.*, 2022, **108**, pp 1179–1196.
[39] Zi, K., Daochun, L., Xiang, J. and Cheng, C. Delaying stall of morphing wing by periodic trailing-edge deflection, *Chin. J. Aeronaut.*, 2020, **33**, pp 493–500.
[40] Wang, L., Feng, L.-H., Liang, Y., Chen, Y.-L. and Li, Z.-Y. Vortex control strategy for unsteady aerodynamic optimization of a plunging airfoil at a low Reynolds number, *Phys Fluids (1994)*, 2021, **33**, p 117110.
[41] Zi, K., Daochun, L., Tong, S., Xiang, J. and Zhang, L. Aerodynamic characteristics of morphing wing with flexible leading-edge, *Chin. J. Aeronaut.*, 2020, **33**, pp 2610–2619.
[42] Andersen, P.B., Gaunaa, M., Bak, C. and Hansen, M.H. A dynamic stall model for airfoils with deformable trailing edges, *Wind Energy: Int. J. Progr. Appl. Wind Power Convers. Technol.*, 2009, **12**, pp 734–751.
[43] Lyu, Z. and Martins, J.R. Aerodynamic shape optimization of an adaptive morphing trailing-edge wing, *J. Aircr.*, 2015, **52**, pp 1951–1970.
[44] Abdessemed, C., Yao, Y., Bouferrouk, A. and Narayan, P. Morphing airfoils analysis using dynamic meshing, *Int. J. Numer. Methods Heat Fluid Flow*, 2018.
[45] Abdessemed, C., Bouferrouk, A. and Yao, Y. Effects of an unsteady morphing wing with seamless side-edge transition on aerodynamic performance, *Energies*, 2022, **15**, p 1093.
[46] Abdessemed, C., Bouferrouk, A. and Yao, Y. Aerodynamic and aeroacoustic analysis of a harmonically morphing airfoil using dynamic meshing, In *Proceedings of the Acoustics*, 2021, pp 177–199.
[47] Kamliya Jawahar, H., Ai, Q. and Azarpeyvand, M. Experimental and numerical investigation of aerodynamic performance of airfoils fitted with morphing trailing-edges, In *Proceedings of the 23rd AIAA/CEAS Aeroacoustics Conference*, 2017, p. 3371.
[48] Jawahar, H.K., Ai, Q. and Azarpeyvand, M. Experimental and numerical investigation of aerodynamic performance for airfoils with morphed trailing edges, *Renew. Energy*, 2018, **127**, pp 355–367.
[49] Wei, B., Gao, Y. and Li, D. Physics of dynamic stall vortex during pitching oscillation of dynamic airfoil, *Int. J. Aeronaut. Space Sci.*, 2021, **22**, pp 1263–1277.
[50] Gupta, R. and Ansell, P.J. Unsteady flow physics of airfoil dynamic stall, *AIAA J.*, 2019, **57**, pp 165–175.
[51] Imamura, T., Enomoto, S., Yokokawa, Y., and Yamamoto, K. Three-dimensional unsteady flow computations around a conventional slat of high-lift devices, *AIAA J.*, 2008, **46**, pp 1045–1053.
[52] Balaji, R., Bramkamp, F., Hesse, M., and Ballmann, J. Effect of flap and slat riggings on 2-D high-lift aerodynamics, *J. Aircr.*, 2006, **43**, pp 1259–1271.
[53] Gerontakos, P. and Lee, T. Dynamic stall flow control via a trailing-edge flap, *AIAA J.*, 2006, **44**, pp 469–480.
[54] Lee, T. and Su, Y. Unsteady airfoil with a harmonically deflected trailing-edge flap, *J. Fluids Struct.*, 2011, **27**, pp 1411–1424.
[55] Traub, L.W., Miller, A., Rediniotis, O., Kim, K., Jayasuriya, S., and Jung, G. Effects of synthetic jets on large amplitude sinusoidal pitch motions, *J. Aircr.*, 2005, **42**, pp 282–285.
[56] Greenblatt, D. and Wygnanski, I. Dynamic stall control by periodic excitation, Part 1: NACA 0015 parametric study, *J. Aircr.*, 2001, **38**, pp 430–438.
[57] Greenblatt, D. and Wygnanski, I.J. The control of flow separation by periodic excitation, *Prog. Aerosp. Sci.*, 2000, **36**, pp 487–545.
[58] Post, M.L. and Corke, T.C. Separation control using plasma actuators: dynamic stall vortex control on oscillating airfoil, *AIAA J.*, 2006, **44**, pp 3125–3135.
[59] Heine, B., Mulleners, K., Joubert, G. and Raffel, M. Dynamic stall control by passive disturbance generators, *AIAA J.*, 2013, **51**, 2086–2097.
[60] Sahin, M., Sankar, L.N., Chandrasekhara, M. and Tung, C. Dynamic stall alleviation using a deformable leading edge concept-a numerical study, *J. Aircr.*, 2003, **40**, pp 77–85.
[61] Popov, A.V., Grigorie, L.T., Botez, R., Mamou, M. and Mébarki, Y. Real time morphing wing optimization validation using wind-tunnel tests, *J. Aircr.*, 2010, **47**, pp 1346–1355.
[62] Bashir, M., Zonzini, N., Botez, R.M., Ceruti, A. and Wong, T. Flow control around the UAS-S45 Pitching Airfoil Using a Dynamically Morphing Leading Edge (DMLE): A numerical study, *Biomimetics*, 2023, **8**, p 51.
[63] Singh, C., Peake, D.J., Kokkalis, A., Khodagolian, V., Coton, F.N. and Galbraith, R.A.M. Control of rotorcraft retreating blade stall using air-jet vortex generators, *J. Aircr.* 2006, **43**, pp 1169–1176.
[64] Ramesh, K., Ke, J., Gopalarathnam, A. and Edwards, J. Effect of airfoil shape and Reynolds number on leading edge vortex shedding in unsteady flows. In *Proceedings of the 30th AIAA Applied Aerodynamics Conference*, 2012, p. 3025.
[65] Kral, L., Donovan, J., Cain, A., Cary, A., Kral, L., Donovan, J., Cain, A. and Cary, A. Numerical simulation of synthetic jet actuators, In *Proceedings of the 4th Shear Flow Control Conference*, 1997, p 1824.
[66] Visbal, M.R. and Benton, S.I. Exploration of high-frequency control of dynamic stall using large-eddy simulations, *AIAA J.*, 2018, **56**, pp 2974–2991.
[67] Visbal, M.R. and Garmann, D.J. Mitigation of dynamic stall over a pitching finite wing using high-frequency actuation, *AIAA J.*, 2020, **58**, pp 6–15.

https://doi.org/10.1017/aer.2023.62 Published online by Cambridge University Press

[68] Sahin, M. and Sankar, L.N. Stall alleviation using a deformable leading edge concept, In *Proceedings of the 2000 IEEE Aerospace Conference. Proceedings (Cat. No. 00TH8484)*, 2000, pp 143–150.
[69] Seifert, A. and Pack, L. Oscillatory excitation of unsteady compressible flows over airfoils at flight Reynolds numbers, In *Proceedings of the 37th Aerospace Sciences Meeting and Exhibit*, 1999, p 925.
[70] Le Pape, A., Costes, M., Richez, F., Joubert, G., David, F. and Deluc, J.-M. Dynamic stall control using deployable leading-edge vortex generators. *AIAA J*, 2012, **50**, pp 2135–2145.
[71] Qijun, Z., Yiyang, M. and Guoqing, Z. Parametric analyses on dynamic stall control of rotor airfoil via synthetic jet, *Chin. J. Aeronaut.*, 2017, **30**, pp 1818–1834.
[72] Visbal, M.R. and Garmann, D.J. Numerical investigation of spanwise end effects on dynamic stall of a pitching NACA 0012 wing, In *Proceedings of the 55th AIAA aerospace sciences meeting*, 2017, p 1481.
[73] Feszty, D., Gillies, E.A. and Vezza, M. Alleviation of airfoil dynamic stall moments via trailing-edge flap flow control, *AIAA J.*, 2004, **42**, pp 17–25.
[74] Lee, T. and Gerontakos, P. Unsteady airfoil with dynamic leading-and trailing-edge flaps, *J. Aircr.*, 2009, **46**, pp 1076–1081.
[75] Gerontakos, P. and Lee, T. Trailing-edge flap control of dynamic pitching moment, *AIAA J.*, 2007, **45**, pp 1688–1694.
[76] Samara, F. and Johnson, D.A. Deep dynamic stall and active aerodynamic modification on a S833 airfoil using pitching trailing edge flap, *Wind Eng.*, 2021, **45**, pp 884–903.
[77] Karimian, S., Aramian, S. and Abdolahifar, A. Numerical investigation of dynamic stall reduction on helicopter blade section in forward flight by an airfoil deformation method, *J. Braz. Soc. Mech. Sci. Eng.*, 2021, **43**, pp 1–17.
[78] Khurana, M., Winarto, H. and Sinha, A. Airfoil geometry parameterization through shape optimizer and computational fluid dynamics, In *Proceedings of the 46th AIAA Aerospace Sciences Meeting and Exhibit*, 2008, p. 295.
[79] Trad, M.H., Segui, M. and Botez, R.M. Airfoils generation using neural networks, CST curves and aerodynamic coefficients, In *Proceedings of the AIAA AVIATION 2020 FORUM*, 2020, p 2773.
[80] Derksen, R. and Rogalsky, T. Bezier-PARSEC: An optimized aerofoil parameterization for design, *Adv. Eng. Softw.*, 2010, **41**, pp 923–930.
[81] Mcallister, K., Carr, L. and Mccroskey, W. Dynamic stall experiments on the NACA 0012 airfoil [Technical report No. 1100], 1978.
[82] Correa, A.F.M. The study of dynamic stall and URANS capabilities on modelling pitching airfoil flows, Masters Thesis, Universidade Federal De Uberlândia, 2015.

Cite this article: Bashir M., Zonzini N., Longtin Martel S., Botez R.M., Ceruti A. and Wong T. (2024). Numerical investigation of the dynamic stall reduction on the UAS-S45 aerofoil using the optimised aerofoil method. *The Aeronautical Journal*, **128**, 441–468. https://doi.org/10.1017/aer.2023.62